# cmgh

ORIGINAL RESEARCH

A Planar Culture Model of Human Absorptive Enterocytes Reveals Metformin Increases Fatty Acid Oxidation and Export

Ismael Gomez-Martinez,[1,*] R. Jarrett Bliton,[2,*] Keith A. Breau,[1] Michael J. Czerwinski,[1] Ian A. Williamson,[5,6] Jia Wen,[5] John F. Rawls,[5] and Scott T. Magness[1,2,3,4]

[1]Department of Cell Biology and Physiology, University of North Carolina at Chapel Hill, Chapel Hill, North Carolina; [2]Joint Department of Biomedical Engineering, University of North Carolina at Chapel Hill/North Carolina State University, Chapel Hill, North Carolina; [3]Department of Medicine, University of North Carolina at Chapel Hill, Chapel Hill, North Carolina; [4]UNC Center for Gastrointestinal Biology and Disease, University of North Carolina at Chapel Hill, Chapel Hill, North Carolina; [5]Department of Molecular Genetics and Microbiology, Duke Microbiome Center, School of Medicine, Durham, North Carolina; and [6]Department of Biomedical Engineering, Woo Center for Big Data and Precision Health, Pratt School of Engineering, Duke University, Durham, North Carolina
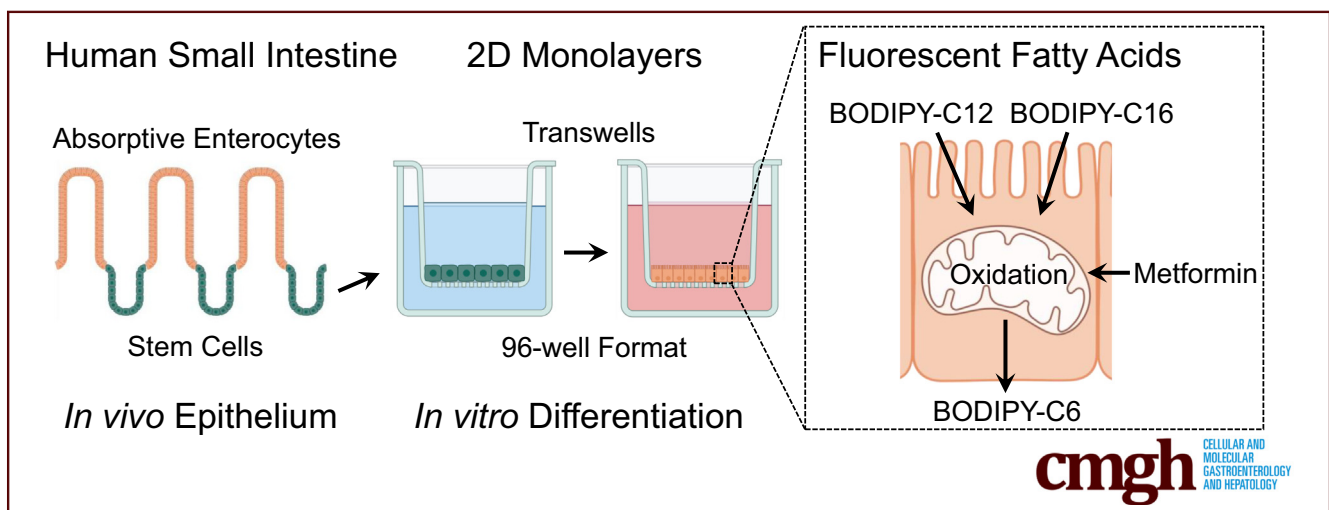
SUMMARY

Single-cell transcriptomics on human enterocytes characterized lipid-handling gene expression patterns that were mimicked in culture. Candidate drugs were tested on a high-throughput 96-well, scale-up system, showing that metformin increases fatty acid oxidation and fatty acid export.

BACKGROUND & AIMS: Fatty acid oxidation by absorptive enterocytes has been linked to the pathophysiology of type 2 diabetes, obesity, and dyslipidemia. Caco-2 and organoids have been used to study dietary lipid-handling processes including fatty acid oxidation, but are limited in physiological relevance or preclude simultaneous apical and basal access. Here, we developed a high-throughput planar human absorptive enterocyte monolayer system for investigating lipid handling, and then evaluated the role of fatty acid oxidation in fatty acid export, using etomoxir, C75, and the antidiabetic drug metformin.

METHODS: Single-cell RNA-sequencing, transcriptomics, and lineage trajectory was performed on primary human jejunum. In vivo absorptive enterocyte maturational states informed conditions used to differentiate human intestinal stem cells

(ISCs) that mimic in vivo absorptive enterocyte maturation. The system was scaled for high-throughput drug screening. Fatty acid oxidation was modulated pharmacologically and BODIPY (Thermo Fisher Scientific, Waltham, MA) (B)–labeled fatty acids were used to evaluate fatty acid handling via fluorescence and thin-layer chromatography.

RESULTS: Single-cell RNA-sequencing shows increasing expression of lipid-handling genes as absorptive enterocytes mature. Culture conditions promote ISC differentiation into confluent absorptive enterocyte monolayers. Fatty acid-handling gene expression mimics in vivo maturational states. The fatty acid oxidation inhibitor etomoxir decreased apical-to-basolateral export of medium-chain B-C12 and long-chain B-C16 fatty acids, whereas the CPT1 agonist C75 and the antidiabetic drug metformin increased apical-to-basolateral export. Short-chain B-C5 was unaffected by fatty acid oxidation inhibition and diffused through absorptive enterocytes.

CONCLUSIONS: Primary human ISCs in culture undergo programmed maturation. Absorptive enterocyte monolayers show in vivo maturational states and lipid-handling gene expression profiles. Absorptive enterocytes create strong epithelial barriers in 96-Transwell format. Fatty acid export is proportional to fatty acid oxidation. Metformin enhances fatty acid oxidation

and increases basolateral fatty acid export, supporting an intestine-specific role. *(Cell Mol Gastroenterol Hepatol 2022;14:409–434;* https://doi.org/10.1016/j.jcmgh.2022.04.009*)*

Keywords: Intestinal Stem Cells; Absorptive Enterocyte Monolayers; Fatty Acid Oxidation; Drug Screening.

See editorial on page 407.

The small intestinal (SI) epithelium is a selective barrier that serves as the point of entry for essential micronutrients and macronutrients to meet energy demands and preserve general homeostatic functions. Lipids are the most energy-dense of the macronutrients and are absorbed by the SI epithelium.[1] The majority of dietary lipids are triglycerides and are broken down by the stomach and intestinal lumen into fatty acids and monoglycerides.[1] Fatty acids then are taken up by absorptive enterocytes, the predominant cell type of the SI epithelium.[1] Lipids then can be metabolized and used by absorptive enterocytes for cellular functions such as energy production, membrane synthesis, and storage as lipid droplets,[2] or distributed to the body by the well-accepted lipoprotein–lymphatic system and by the less-appreciated fatty acid–portal vein pathway.[3–5]

Investigating uptake, metabolism, and export of dietary fatty acids, here collectively called *fatty acid handling*, in vitro is challenging because of the historical lack of physiologically relevant culture models. Because metabolic disorders such as dyslipidemia, diabetes, and obesity[1,6,7] are increasing,[8,9] there is strong interest in evaluating how genetics[2,10,11] and environmental factors, such as alterations in gut microbiota[12–15] and eating behaviors,[1,6,7] are associated with fatty acid–handling mechanisms, which by nature are complex to study in human beings or animal models. Limitations of 3-dimensional organoid cultures, ethical considerations of human research, and inadequacies of animal models compound the challenges and limit scientific progress toward solutions for these and other metabolic diseases. In this regard, an absorptive enterocyte cell culture platform using primary human cells and coupled with simple and sensitive detection of fatty acids and their metabolites would represent a significant improvement and address many of the limitations of existing in vitro culture models.

Traditionally, cell culture models of human SI epithelium largely have relied on cancer or transimmortalized mouse intestinal cell lines (ie, Caco-2,[16] m-ICcl2,[17] and so forth), which retain properties consistent with undifferentiated states.[18–20] Organoid culture models have become popular alternatives because they typically are derived from primary intestinal epithelial stem cells (ISCs) and can differentiate into the main mature lineages of the differentiated gut epithelium.[21,22] Organoids are small (diameter, ∼100–1000 μm) spherical structures cultured in thick hydrogels. They are composed of polarized cells in which the enclosed apical or luminal surface precludes application of fatty acids to the physiologically relevant surface to mimic dietary absorption.[22] Organoids can be cultured with the apical surface facing outward (apical-out organoids)[23]; however, this causes the basal surface to be enclosed and inaccessible, preventing sampling of exported or metabolized lipids. Collectively, these factors limit interpretations, reduce throughput, and prohibit analyses necessary to accurately assess fatty acid handling across the absorptive enterocyte monolayer.

Conventional methods to detect fatty acids has relied on using radioisotope- and heavy isotope–labeled fatty acid analogs.[24–30] These isotope-labeled fatty acids are thought to behave similarly to native fatty acids in absorptive, metabolic, and export processes[24–30]; however, special safety precautions and sophisticated downstream analytics (eg, mass spectrophotometry) are required, limiting access of these assays to many investigators. Fluorescently labeled fatty acids represent an attractive alternative because they do not require special handling, are sensitive, commercially available, and can be detected using a variety of common instruments and methods (eg, plate readers, microscopes, thin layer chromatography [TLC]).[31] For example, BODIPY (Thermo Fisher Scientific, Waltham, MA) (B) is a brightly fluorescent fluorophore, and B-fatty acid analogs have been shown to mimic endogenous fatty acid metabolism and transport, making it an effective tracer for fatty acids in lipid-handling studies.[31–35] Importantly, unlike isotopically labeled fatty acids, fluorescently labeled fatty acids also permit imaging of fatty acid handling in live and fixed cells.[34,35]

Our group recently developed methods for culturing and indefinitely expanding primary human ISCs as 2-dimensional (2D) monolayers.[36] ISCs cultured this way then can be transferred to Transwell (Corning, Corning, NY) inserts, cultured to confluence, and then terminally differentiated into absorptive and secretory lineages found in vivo.[36,37] Monolayers cultured on permeable Transwell inserts are in contact with apical and basal reservoirs where factors, drugs, and metabolites easily can be added or sampled throughout an experiment.[36] Unlike organoids, monolayers grow as planar sheets rather than spheres suspended in thick hydrogels, allowing use of imaging systems that are in common use in basic science laboratories, robotic drug screening, and validation platforms.

 Most current article

Our study here had 2 primary goals: the first was to develop and validate a new culture system to study fatty acid handling, and the second was to use the system to show utility for evaluating the impact that a set of drugs has on fatty acid oxidation and export of fatty acid metabolites. We took an approach that first defined the baseline transcriptomic state of relevant lipid-handling genes and then tailored culture conditions to mimic the in vivo lipid-handling gene profiles. Readouts for fatty acid handling are designed for practicality, sensitivity, and high-throughput applications. Using this new system, we pharmacologically inhibited and potentiated fatty acid oxidation and observed changes in fatty acid export that informed a hypothesis that fatty acid oxidation increases export of medium- and long-chain fatty acid metabolites across the basolateral membrane. This was tested and the findings showed new biological insights into the role of fatty acid oxidation on export of fatty acids with implications for understanding blood-glucose regulation and appetite control.

Results

Single-Cell Transcriptomics of Jejunal and Ileal Human Mucosa Define Early, Intermediate, and Mature Nutrient-Handling Enterocytes

First, we sought to characterize the baseline transcriptomic profiles of human absorptive enterocytes in vivo to guide the development of an in vitro model of human fatty acid handling. The distal SI (jejunum and ileum) represents the majority of absorptive epithelium in the human SI[38]; however, lipid-handling transcriptional profiles of jejunal and ileal absorptive lineages have not been fully described at the single-cell level. Endoscopic biopsy specimens have enabled single-cell transcriptomics to be performed on human duodenal[39] and ileal[40] mucosa; however, single-cell transcriptomics only recently have been reported for the jejunum,[41,42] with limited characterization of absorptive function.[38,42] To further define absorptive function of the distal SI, single-cell RNA-sequencing (scRNAseq) was performed on primary jejunal and ileal epithelium isolated from a healthy organ donor. To identify the distinct cell types captured in the data set, dimensional reduction was performed,[43] showing that the cell populations represented the major reported cell lineages in the human SI epithelium[39] (Figure 1A). Most cells in the data set clustered separately from the minority secretory lineages (enteroendocrine, goblet, bestrophin 4 (BEST4)+, and tuft). This main cluster comprised cells consistent with ISCs, transit-amplifying cells, and absorptive enterocytes (Figure 1A). The high viability, quality, and capture of the full complement of major SI epithelial lineages provided a strong foundation for transcriptomic characterization.

In human duodenum and ileum, absorptive enterocytes are subcategorized as early, intermediate, and mature based on maturation state.[39,45] Genes associated with these 3 absorptive enterocyte subsets also were observed in jejunal and ileal Leiden clustering (Figure 1A). Jejunal and ileal absorptive enterocytes clustered together, showing a high degree of transcriptomic similarity between these cells.

Because Leiden-cluster boundaries appear artificially binary, each cell was interrogated independently using a computational score comprising curated gene sets that would predict cell lineages for each Leiden cluster. Three different curated gene sets from prior studies were used to identify different cell-cycle stages,[46] ISCs,[44,47,48] and absorptive enterocytes[40] (Figure 1B–D). The cell-cycle score showed that most cycling cells are associated strongly at one end of the cluster, which is consistent with cells showing the strongest ISC score (Figure 1B and C). By contrast, cells with the highest absorptive enterocyte score were associated strongly with the opposite end of the same cluster (Figure 1D). Twenty ISC signature genes that were reported to be the most highly expressed genes in human ileal ISCs[40] also were highest in jejunal ISCs (Figure 1E). These ISC-associated genes gradually decreased in jejunal absorptive enterocyte populations consistent with differentiation (Figure 1E). Conversely, 20 of the most highly expressed absorptive enterocyte signature genes identified in human ileal mature absorptive enterocytes[40] were lowest in jejunal ISCs. These absorptive enterocyte-associated genes gradually increased in jejunal absorptive enterocyte populations as they differentiated (Figure 1F). Together, these data suggest jejunal absorptive enterocytes follow a similar maturation trajectory as duodenal and ileal cells from other reports.[39,40,45]

Computational Lineage Trajectory Analyses Show Human Absorptive Enterocytes Progress Through Maturation Stages With Increasing Fatty Acid-Handling Gene Expression

A recent study of murine jejunal villi described an absorptive enterocyte maturation program wherein spatially distinct zones along the villus were used to define absorptive enterocyte functions (eg, antimicrobial functions toward the base, lipoprotein secretion toward the tip).[49] Whether human absorptive enterocytes also progress through maturation states corresponding to distinct functions along the length of the villus is unknown. Progressive expression of mature absorptive enterocyte markers in our jejunal data set (Figure 1F) led to the hypothesis that human absorptive enterocyte clusters correspond to lineages with distinct gene expression profiles of maturation along the villus. To test this hypothesis, we used a computational framework based on the rate of change of spliced and unspliced messenger RNA ratios (ie, RNA velocity)[50] and a differentiation-specific RNA velocity-based metric (ie, latent time) (Figure 1G and H).[51] Human jejunal cells were used in the analysis to be consistent with previous mouse studies.[49] Vectors calculated based on the solved dynamic model of RNA velocity predict a trajectory of ISCs gradually differentiating to mature absorptive enterocytes (Figure 1G, arrows). Next, a latent time value between 0 and 1 was assigned to each cell to order cells along the trajectory modeled by the RNA-velocity vectors (Figure 1H). A latent time of 0 means that the cell has yet to enter the modeled trajectory, whereas a latent time of 1 means that the cell has progressed completely through the modeled differentiation pathway. Through combining RNA velocity and latent time,

we show a single path of likely cell transitions from ISCs into early absorptive enterocytes, followed by intermediate absorptive enterocytes, and culminating with mature absorptive enterocytes (Figure 1*G* and *H*).

To visualize the number of differentially expressed genes (DEGs) between these maturation states (ie, early absorptive enterocyte, intermediate absorptive enterocyte, and mature absorptive enterocyte), the 1537 identified DEGs
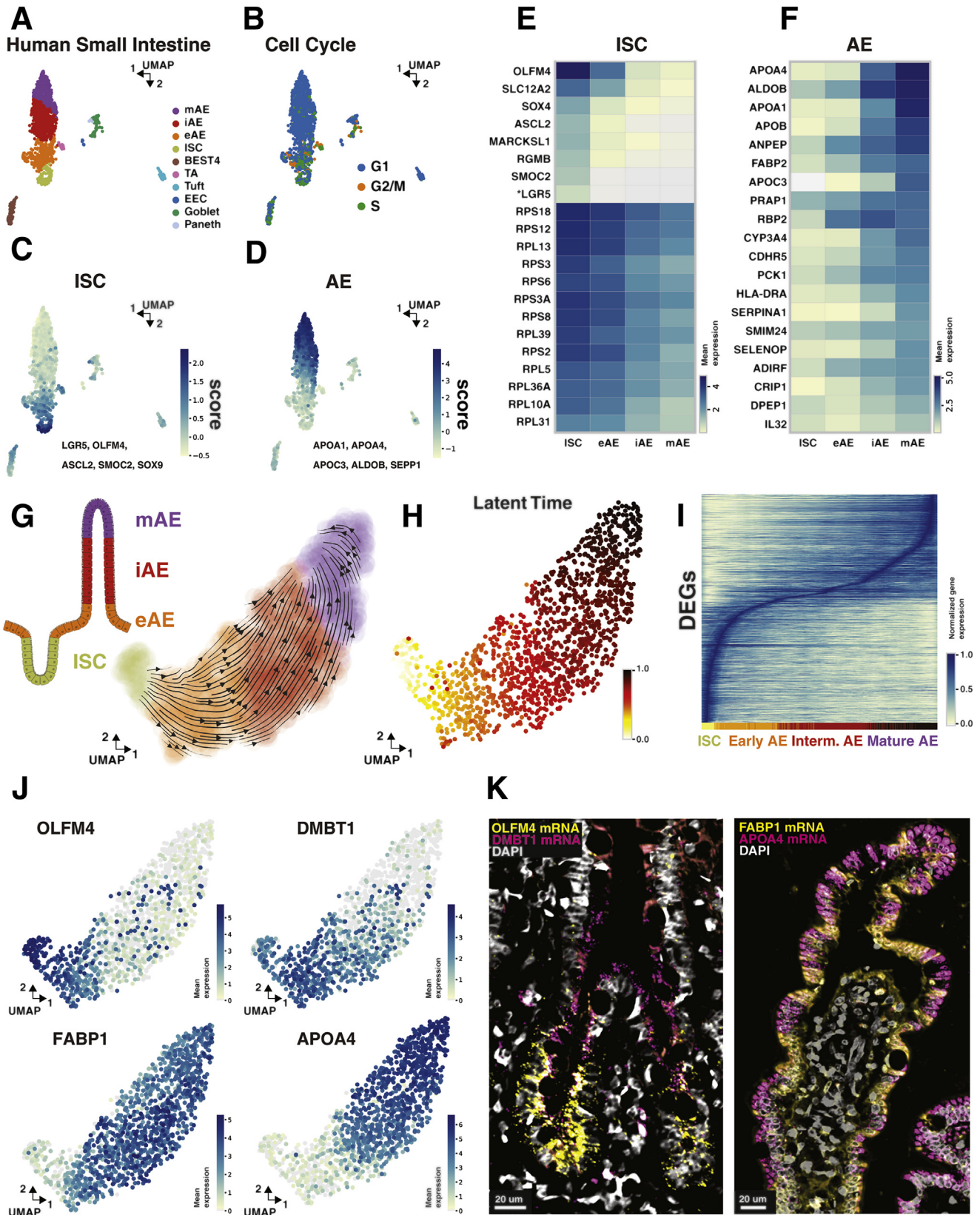
from these populations were plotted against all jejunal ISCs, early absorptive enterocytes, intermediate absorptive enterocytes, and mature absorptive enterocytes as ordered by the calculated latent time (Figure 1*I*, Supplementary Table 1). ISCs and mature absorptive enterocytes had the largest amount of DEGs (732 and 592, respectively), with early absorptive enterocytes and intermediate absorptive enterocytes only having 106 and 107 DEGs, respectively (Supplementary Table 3). The pattern of gene expression showed that genes highest in ISCs gradually turn off as the cells mature (Figure 1*I*). Conversely, mature absorptive enterocyte genes begin to turn on in the early absorptive enterocyte and intermediate absorptive enterocyte states (Figure 1*I*).

In situ hybridization was performed on jejunal tissue sections from the same donor to validate the predicted computational trajectory by locating marker genes for each maturation stage to points along the villus (Figure 1*J* and *K*). Consistent with our predictions, *OLFM4* (ISC marker) localized to the crypt base, *DMBT1* (antimicrobial function) was found in the upper crypt and lower villus, *FABP1* (lipid chaperone) was enriched in the midvillus region, and *APOA4* (chylomicron assembly) was enriched at the villus tip (Figure 1*K*). Consistent with findings in mice, human absorptive enterocytes appear to perform distinct functions as they differentiate along the crypt–villus axis.[49]

The cell maturation analyses were further refined next by using curated gene sets specific for fatty acid handling (Figure 2). Expression of genes associated with chylomicron assembly (*APOA1*, *APOA4*, *APOB*) were enriched in intermediate absorptive enterocyte and mature absorptive enterocyte populations, while distinct subsets of genes involved in regulating fatty acid transport (*CD36*, *SLC27A1*, *SLC27A5*) and fatty acid oxidation (*CPT1A*, *PPARG*, *PPARGC1A*) were enriched differentially in each maturation state, suggesting discrete regulation of these lipid-handling mechanisms along the villi (Figure 2). Together, these findings support distinct transcriptional states and associated lipid-handling mechanisms with each absorptive

enterocyte maturation stage along the crypt–villus axis in the human jejunum.

Characterization of Culture Model by scRNAseq Shows Differentiation of Human Jejunal ISCs Generates Highly Pure Monolayers of Absorptive Enterocytes

In prior work, our group developed platforms that promote robust, long-term expansion of human ISCs.[36] When cultured on Transwell culture systems, ISCs can be induced to differentiate into absorptive enterocytes with strong barrier function and used for transport studies[37,52] (Table 1). The Transwell membrane allows for application and retrieval of fatty acids and their metabolites from the apical and basal reservoirs, respectively. Both are crucial parameters not available in organoids that enable mechanistic studies of fatty acid handling in vitro.

To define cell phenotypes and characterize lineage purity at single-cell resolution, scRNAseq was performed on ISCs under expansion conditions[52] (Figure 2) and absorptive enterocyte monolayers after 5 days of differentiation (Figure 3*A*). Inhibition of Notch signaling is required for specification of the secretory lineage.[53,54] Because we initiated differentiation by removal of ISC growth factors without addition of a Notch inhibitor, we hypothesized that ISCs would follow an absorptive rather than secretory differentiation trajectory. Leiden clustering of ISC expansion and differentiation conditions showed 2 distinct clusters unique to each media formulation (Figure 3*B*). Forty percent of cells in the ISC cluster were predicted by computational methods to be in either S or G2/M phase, whereas more than 99% of cells in absorptive enterocyte differentiation conditions were predicted to be in G0/G1 phase (Figure 2*C*).

Computational cell-cycle predictions cannot distinguish between cells in G1 phase or cells that have left the cell cycle; thus, scoring of ISC and absorptive enterocyte gene profiles was performed to assess if differentiation

---

Figure 1. (*See previous page*). **Single-cell transcriptomics of healthy human absorptive epithelium.** (*A–D*) Unbiased Leiden clustering of primary jejunum and ileum. (*A*) Identification of cell types. (*B*) Inferred cell-cycle state based on expression of previously categorized G1, G2M, and S phase–associated genes.[44] (*C*) ISC score based on expression of established ISC genes *LGR5*, *OLFM4*, *ASCL2*, *SMOC2*, and *SOX9*. (*D*) Absorptive enterocyte score based on expression of established absorptive enterocyte genes *APOA1*, *APOA4*, *APOC3*, *ALDOB*, and *SEPP1*. (*E* and *F*) Gene expression of ISCs, and absorptive enterocyte populations identified in panel *A*. (*E*) Expression of top 20 ISC genes previously identified in human ileum.[41] *LGR5* was not within the top 20 ISC genes previously identified in human ileum, but it was included for reference. (*F*) Expression of top 20 absorptive enterocyte genes previously identified in human ileum.[41] (*G*) *Bottom right*: Vectors calculated based on a dynamic model of RNA velocity showing likely cell transitions of ISCs, early absorptive enterocytes, intermediate absorptive enterocytes, and mature absorptive enterocytes. *Top left*: Schematic showing likely positions of identified ISCs and absorptive enterocyte populations along the crypt–villus axis. Note that secretory and ileal lineages were removed from the analysis to focus on the relationship between ISCs and maturing of jejunal absorptive enterocytes. (*H*) A latent time value between 0 and 1 was assigned to each cell to order cells along the trajectory modeled by RNA velocity. A latent time of 0 means that the cell has yet to experience any differentiation in the modeled trajectory whereas a latent time of 1 means that the cell has progressed completely through the modeled differentiation pathway. (*I*) Identified human jejunal absorptive enterocytes were ordered based on latent time (x-axis) and DEGs of identified human ISCs and absorptive enterocyte populations were plotted on the y-axis. *LGR5* was not among the top 20 ISC genes identified in human Ileum.[41] (*J*) UMAPs showing expression of select DEGs from the population of cells along the ISC to mature absorptive enterocyte differentiation axis. (*K*) In situ hybridization of ISCs and early absorptive enterocyte DEGs *OLFM4* and *DMBT1*, respectively (*left*). In situ hybridization of intermediate absorptive enterocyte and mature absorptive enterocyte DEGs FABP1 and *APOA4*, respectively (*right*). AE, absorptive enterocyte; DAPI, 4′,6-diamidino-2-phenylindole; mRNA, messenger RNA; UMAP, uniform manifold approximation and projection.
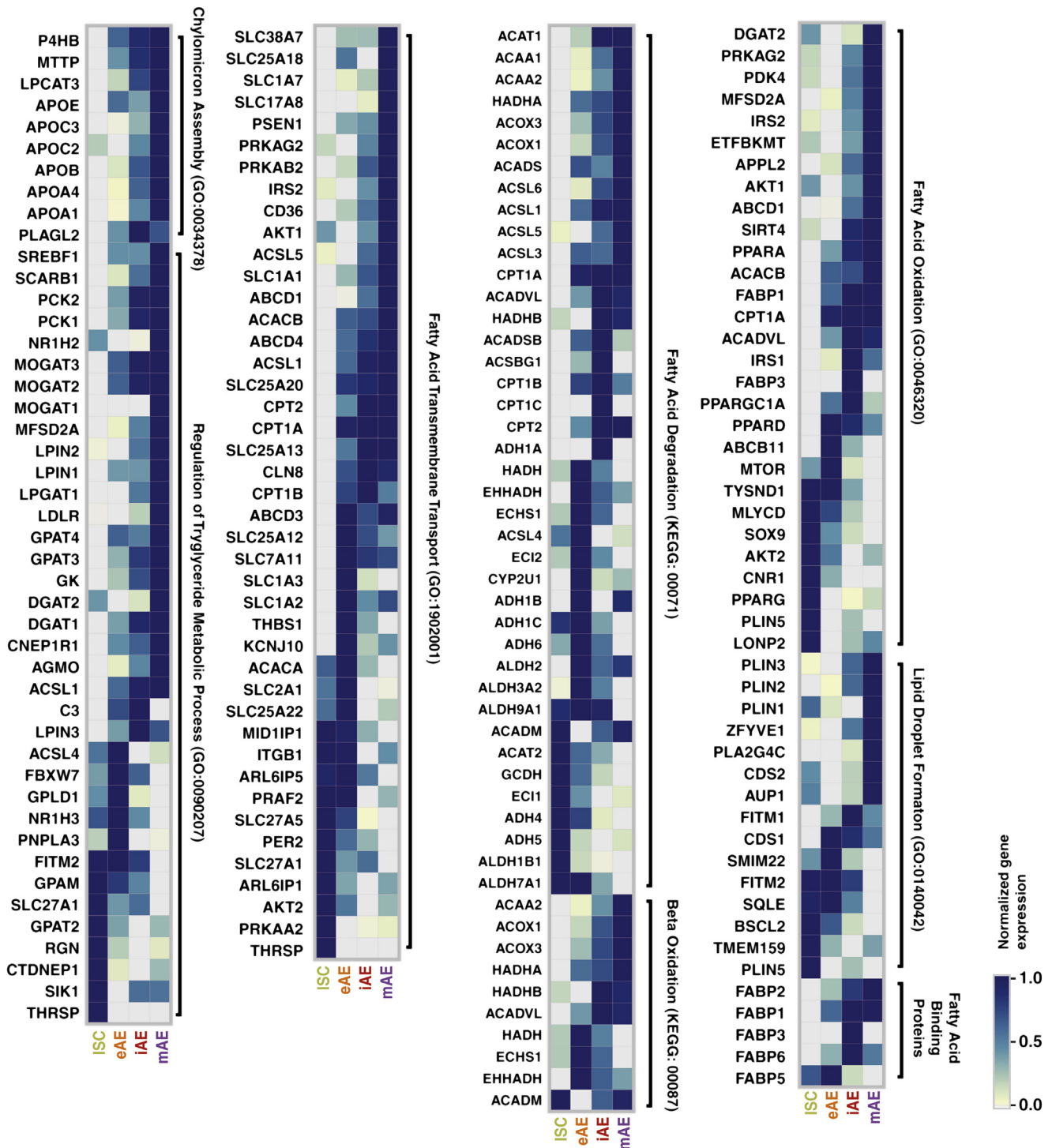
Figure 2. Expression of lipid-handling genes in in vivo ISCs and human absorptive enterocyte populations. Genes were selected from Gene Ontology (GO) terms relating to lipid metabolic processes. Fatty acid binding protein genes were selected manually and not derived from GO terms (*bottom* left). The following genes were not detected in our data set and were excluded: *DGAT2L7P, MIR29B1, MIR30C1, MIR548P, APOA2, PLIN4, ABCD2, GRM1, NTSR1, SLC17A6, SLC17A7, SLC1A6, ABCD2,* and *TWIST1.*

conditions were sufficient to confer terminal differentiation toward an absorptive fate (Figure 2D). ISC and absorptive enterocyte scores were generated for cells grown in in vitro monolayers using curated gene sets that identify either ISCs or absorptive enterocytes (Figure 3D). This scoring showed that in vitro monolayers had higher expression of ISC genes in expansion conditions and higher expression of absorptive enterocyte genes in differentiation conditions (Figure 3D).

Table 1. Tissue Culture Media Conditions

Reagent	Stock solution	EM	DM
L-WRN–conditioned medium		50%	
Advanced DMEM/F12	1×	50%	100%
Glutamax	100×	1×	1×
HEPES	1 mol/L	10 mmol/L	10 mmol/L
Primocin	50 mg/mL	50 ug/mL	50 ug/mL
N-acetyl-cysteine	1 mol/L	1 mmol/L	1 mmol/L
Murine EGF	250 ug/mL	50 ng/mL	50 ng/mL
Nicotinamide	1 mol/L	10 mmol/L	
B27	50×	1×	
Gastrin	1 mg/mL	10 nmol/L	
PGE2	1 mmol/L	10 nmol/L	
A8301	5 mmol/L		500 nmol/L
SB202190	30 mmol/L	3 umol/L	
Y27632	10 mmol/L	10 umol/L	

EGF, epidermal growth factor; L-WRN, L-cell derived Wnt3a, R spondin 3, and Noggin; PGE2, prostaglandin E2.
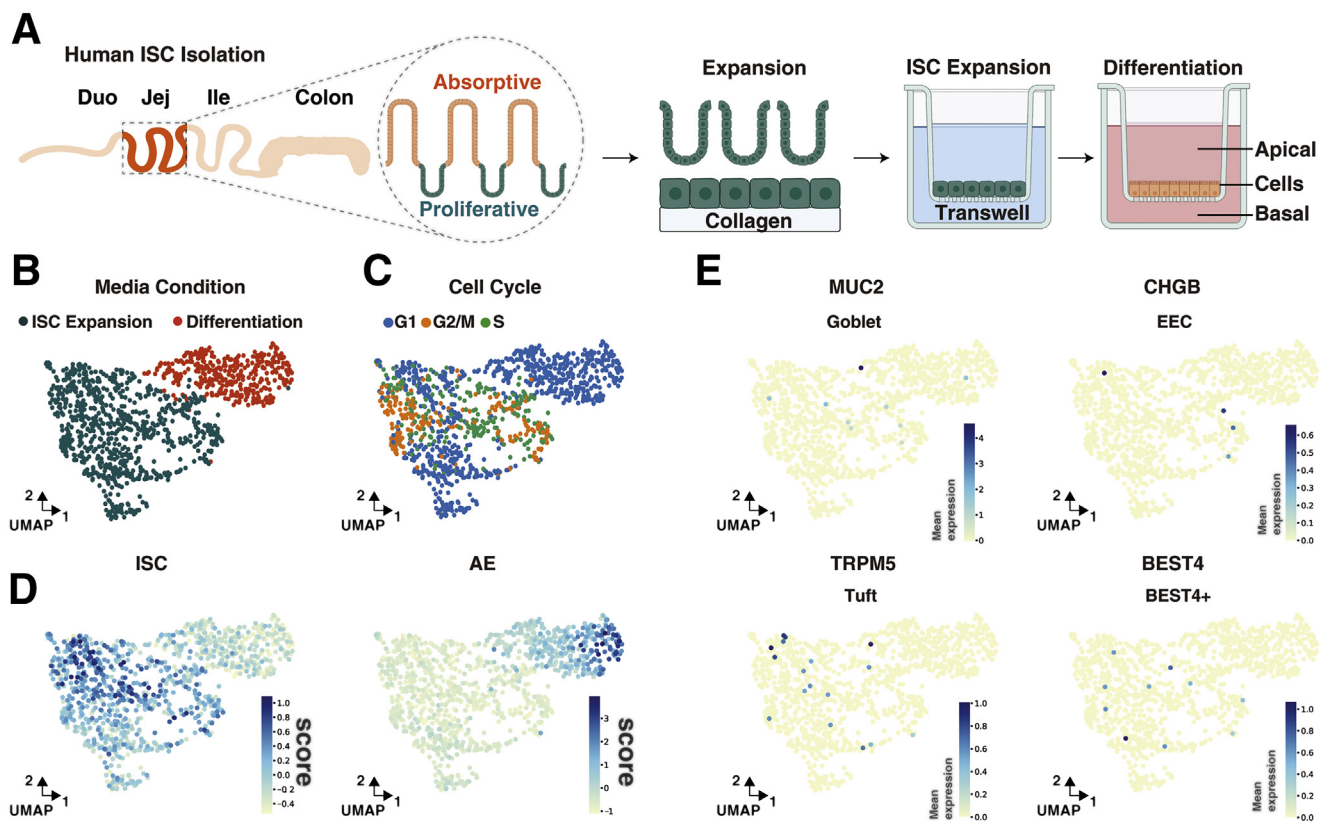

Figure 3. Single-cell transcriptomics of 2D ISCs and absorptive enterocyte cultures. (A) Schematic of isolation, expansion, and differentiation of ISCs from the jejunum of a healthy organ donor. (B) Unbiased Leiden clustering of collagen-grown ISCs (green) and ISCs differentiated for 2 days (orange). (C) Inferred cell-cycle state based on expression of previously categorized G1, G2M, and S phase–associated genes.[44] (D) *Left*: ISC score based on expression of established ISC genes *LGR5*, *OLFM4*, *ASCL2*, *SMOC2*, and *SOX9*. *Right*: Absorptive enterocyte score based on expression of established absorptive enterocyte genes *APOA1*, *APOA4*, *APOC3*, *ALDOB*, and *SEPP1*. (E) Expression of secretory lineage markers *MUC2*, *CHGB*, *TRPM5*, and *BEST4*. AE, absorptive enterocyte; BEST4, bestrophin 4; CHGB, chromagranin B; Duo, duodenum; EEC, enteroendocrine cell; Ile, ileum; Jej, jejunum; MUC2, mucin2; TRPM5, Transient Receptor Potential Cation Channel Subfamily M Member 5; UMAP, uniform manifold approximation and projection.
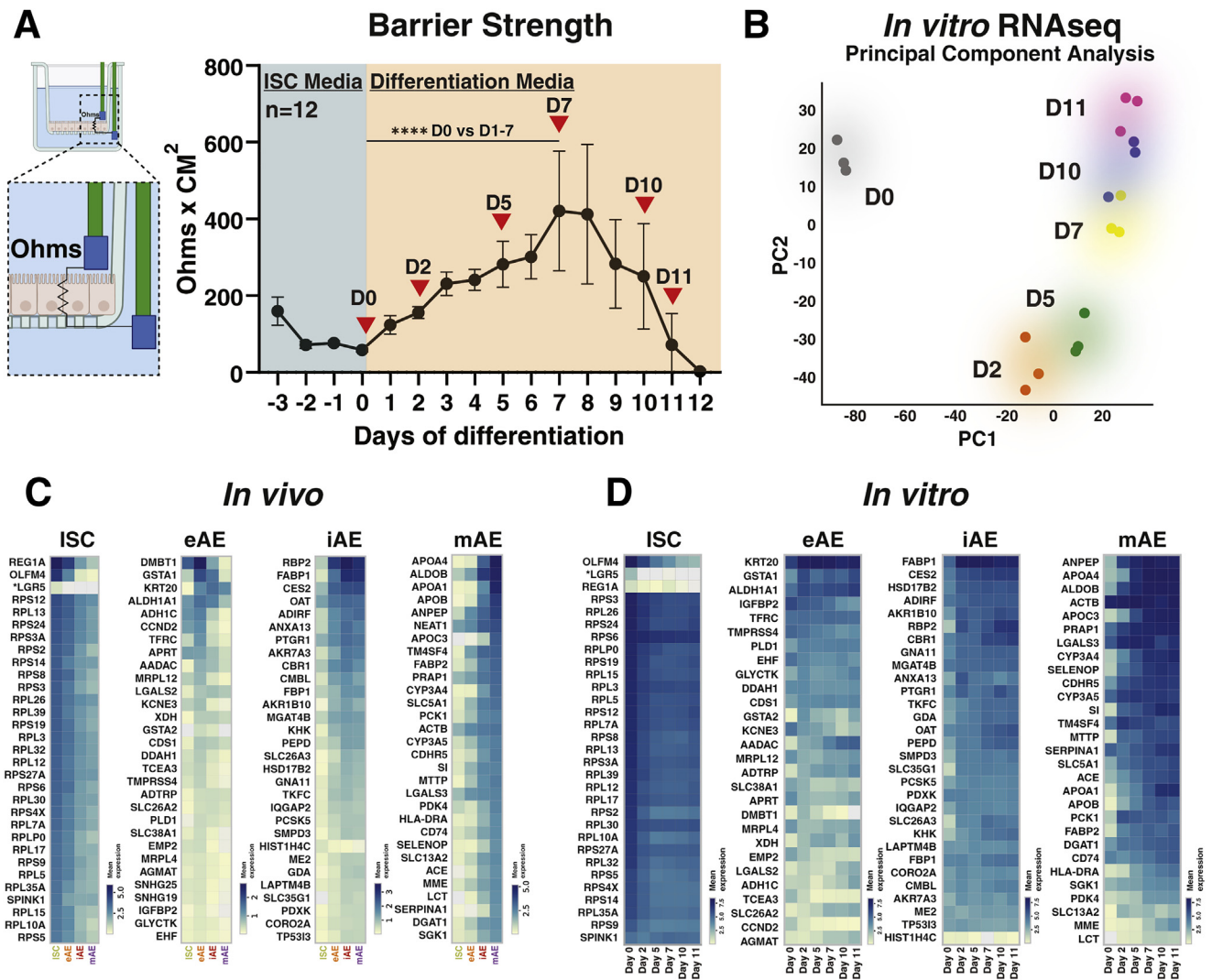
Figure 4. RNAseq shows a time-dependent absorptive enterocyte maturation program in jejunal ISCs in vitro. (A) TEER of jejunal ISCs (n = 12 Transwell cultures). ISCs were maintained in expansion media for 3 days and then switched to differentiation media for 12 days. TEER was monitored daily. *Red triangles* indicate time points at which cells were lysed for bulk RNAseq. A Kolmogorov–Smirnov test was performed comparing TEER between day 0 (D0) and D1–D7. ****$P < .0001$. (B) Principal component analysis of sequenced transcriptomes. (C) Expression of the top 30 DEGs in ISCs, early absorptive enterocytes, intermediate absorptive enterocytes, and mature absorptive enterocytes. (D) In vitro expression of the top 30 in vivo ISC, early absorptive enterocyte, intermediate absorptive enterocyte, and mature absorptive enterocyte DEGs. *SNHG19*, *SNHG25*, and *NEAT1* were not detected in our in vitro data set and were excluded. *LGR5 was not among the top 30 DEGs in ISCs but it was included for reference.

Very rare cells expressing markers of classic secretory lineages (goblet cells, enteroendocrine cells, tuft cells, BEST4+ cells) were observed (Figure 3E). These data show that culture conditions promoted ISC differentiation toward an absorptive cell fate and indicate the potential to model physiological absorptive enterocyte differentiation in vitro.

Culture Methods Developed in 96-Transwell Format Drive Time-Dependent ISC Differentiation and Absorptive Enterocyte Maturation Described by Transcriptomic States

Absorptive enterocyte planar monolayers were scaled to a 96-well Transwell format for high-throughput applications. Transepithelial electrical resistance (TEER) was used to monitor barrier integrity[55] over 15 days of ISC expansion (4 days) and absorptive enterocyte differentiation (12 days) (Figure 4A). As expected,[56] ISC conditions produced a stable and low TEER, while differentiation media (DM) produced an immediate and progressive increase in TEER that peaked at 7 days of differentiation (Figure 4A). The progressive increase in TEER suggests changes in gene expression patterns consistent with mature absorptive enterocytes. To confirm this at the transcriptomic level, bulk RNAseq was performed on absorptive enterocytes in differentiation conditions for 0, 2, 5, 7, 10, and 11 days (Figure 4B). Principal component analysis showed tight agreement between technical replicates and showed rapid

and large transcriptomic changes after just 2 days of differentiation (Figure 4B). Bulk RNAseq of absorptive enterocyte monolayers showed a trajectory of progressive transcriptional changes through time (Figure 4B). Top in vivo DEGs (Figure 4C) were expressed at corresponding maturation time points in vitro (Figure 4D), suggesting an intrinsic program of progressive absorptive enterocyte maturation that begins upon removal of ISC niche growth factors.

To further determine the optimal time points to investigate fatty acid handling (ie, fatty acid transmembrane transport, fatty acid oxidation, lipid droplet formation, chylomicron secretion, and triglyceride metabolic processes), the expression of key genes in these processes was evaluated. There was a general increase in fatty acid–handling genes as cells matured both in vivo and in vitro (Figure 5A). Linear correlation was used to quantitatively describe the extent of similarity between in vivo and in vitro fatty acid–handling gene expression during absorptive enterocyte maturation (Figure 5A and B). Pairwise comparisons of mean lipid-handling gene expression values showed that absorptive enterocytes on day 7 are more similar to intermediate and mature absorptive enterocytes than ISCs and early absorptive enterocytes (Figure 5A and B). Thus, TEER and expression profiles of key fatty acid handling genes were used as criteria to inform the optimal window to investigate fatty acid handling within our model system. Based on these criteria, 7 days of differentiation was the only time point to show both high TEER and close similarity to in vivo mature absorptive enterocyte gene expression of fatty acid–handling genes. For this reason, we chose to assay fatty acid handling in differentiated absorptive enterocytes after 7 days of directed differentiation.

High-Throughput Planar Absorptive Enterocyte Cultures Produce Robust Epithelial Barriers and Preserve Fatty Acid–Handling Functions Detected by Fluorescent Fatty Acid Conjugates

High TEER and transcriptomic data suggest that absorptive enterocyte monolayers could serve as an effective in vitro model for human absorptive enterocyte lipid handling. Strong barrier function is required for accurate interpretation of fatty acid handling by absorptive enterocytes because a leaky barrier would allow fatty acids to bypass the absorptive enterocyte monolayer. As a means to provide sensitive readouts for fatty acid handling that is accessible to most laboratories, we adopted fluorescent analogs that can be detected easily by a fluorescent plate reader and TLC. To validate barrier function, 10 kilodaltons of dextran conjugated to Alexa Fluor 647 (Dextran-647), a nonabsorbable fluorescent polysaccharide, was applied to the apical monolayer surface, followed by quantification of basolateral fluorescence at 2, 4, and 6 hours of apical exposure (Figure 6A). There were nearly undetectable levels of Dextran-647 (<0.2 pmol) in the basal reservoir at any time point, whereas Transwells without cells allowed more

than 30 pmol to diffuse through and reached an equilibrated concentration within approximately 4 hours. These data show strong barrier function and that significant epithelial barrier defects can be detected readily by a Dextran-647 signal in the basal reservoir as early as 2 hours after exposure.

BODIPY (B) is a bright fluorophore that has a different fluorescent signature than Dextran-647, facilitating separate detection of these 2 molecules by plate readers. B–fatty acid analogs have been used extensively for lipid trafficking and metabolism studies in vitro and in vivo and are considered to be handled accurately by absorption, metabolism, and export mechanisms.[58–62] Thus, to characterize fatty acid–handling properties of absorptive enterocyte monolayers, we applied the medium-chain fatty acid analog B-C12 to the apical surface of absorptive enterocyte cultures for 6 hours (Figure 4B). Apical (input) and basal (output) media were collected, and absorptive enterocytes were lysed after 6 hours of apical exposure (Figure 4B). TLC was used to detect and quantify input of B–fatty acids as well as metabolized and exported B–fatty acid products. A combination of polar and protonating solvents were used to resolve the complex mixture of B–fatty acids and metabolites (Figure 6D and E). B-labeled fatty acid standards were applied to the TLC plate in a separate lane and unknown fatty acid species of different carbon chain lengths were extrapolated (Figure 6C). These methods were scaled for the 96-well Transwell system using less than 170 μL media or cell lysate. A previous study[62] using TLC to identify B-lipid species with the same solvents used in this study reported naturally fluorescent bands (NFBs) that do not correspond to B-lipids (Figure 6D and E). TLC showed clear separation of key fatty acid species in all 3 reservoirs (ie, apical, cellular, basal), indicating robust sensitivity of this approach for detection of a broad range of fatty acid species (Figure 6D).

To evaluate fatty acid handling by absorptive enterocyte monolayers, B-C12 was incubated with absorptive enterocyte monolayers for 6 hours followed by TLC analysis to identify the B–fatty acid or B-metabolites in each reservoir (ie, apical, cellular, basal). TLC showed that most of the B-labeled species in the apical reservoir were medium-chain fatty acids (B-C12, B-C8, and B-C6) (Figure 6D and E). A short-chain species consistent with B-C4 also was detected in the apical reservoir at a lower level (Figure 6D and E). In the intracellular reservoir, the largest species were triglycerides, indicating robust fatty acid esterification, and phospholipids indicative of B-C12 being metabolized and incorporated into the lipid bilayers.[57] In the cell lysates, fatty acids were some of the lowest B-lipid species, suggesting dynamic metabolism, diffusion, and mobilization. In the basal reservoir, fatty acids were the predominant B-lipid species, with a smaller fraction consisting of triglycerides, suggesting basal export of fatty acids and chylomicrons (Figure 6D and E). Together these data show robust detection of input B-fatty acids, a broad range of the derivative metabolites, and their relative distributions in each reservoir as the B-lipids are processed by absorptive enterocytes.
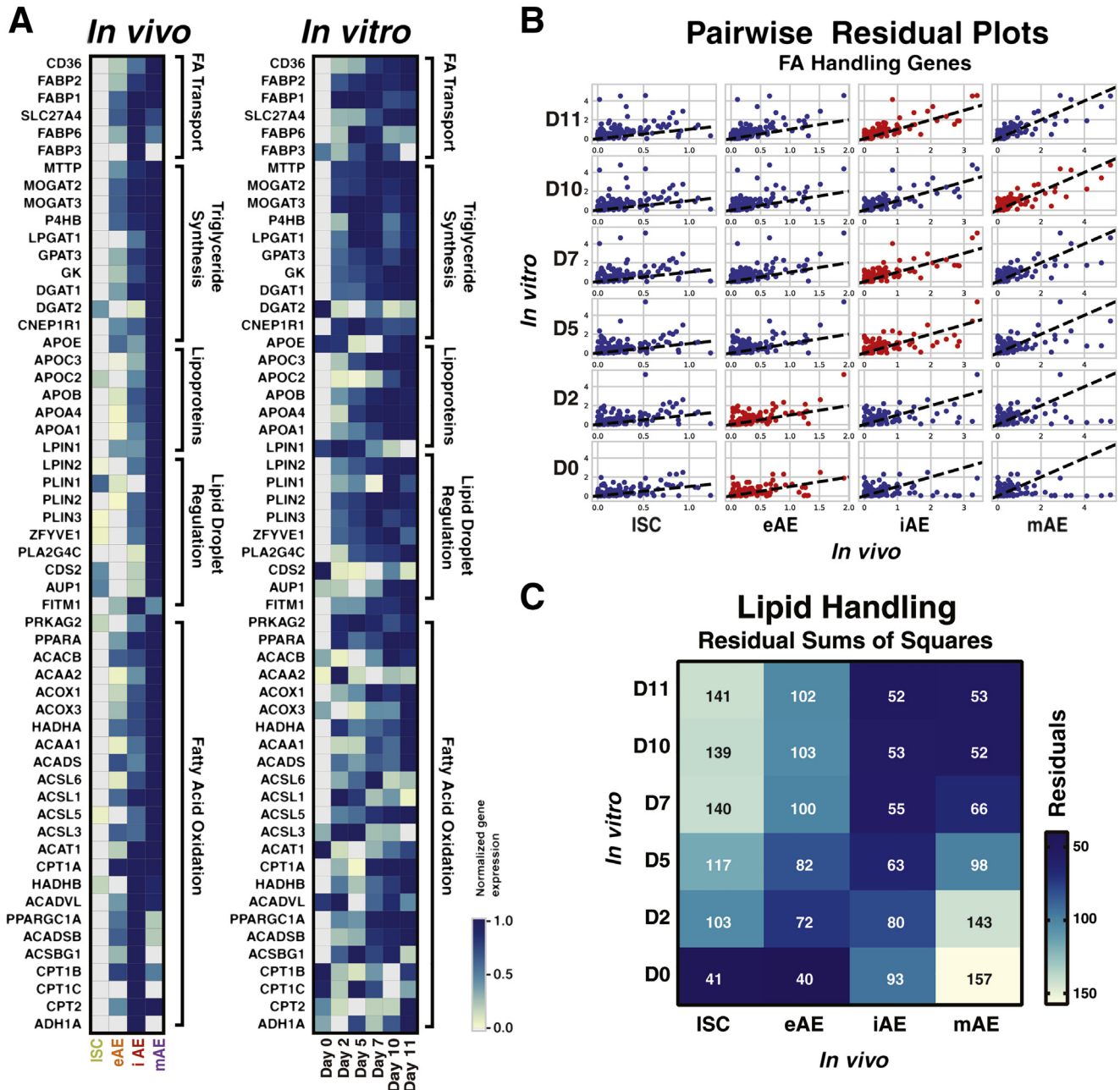
Figure 5. RNAseq shows a time-dependent lipid-handling program in jejunal ISCs in vitro. (*A*) Expression of a curated set of fatty acid–handling genes in vivo (*left*) and in vitro (*right*). Genes were curated from the genes in Figure 2. (*B*) Matrix showing linear regression plots for lipid-handling genes. Each *dot* represents the mean expression for a lipid-handling gene. The x-axis represents the mean (n = 3 samples per time point) expression from in vitro bulk RNAseq data. The y-axis represents the mean expression for each cluster from in vivo scRNAseq data. The *dotted line* shows the line that was used to calculate residuals and is drawn with slope = 1 (ie, mean expression of in vitro differentiation bulk RNAseq data perfectly matches in vivo scRNAseq mean expression for each cluster). *Red dots* indicate the lowest residual sum of squares for each row (ie, lowest residual for each time point sampled in the in vitro differentiation experiment). (*C*) Residual plot of key lipid-handling genes. FA, fatty acid.

Inhibiting Fatty Acid Oxidation in Absorptive Enterocyte Monolayers Decreases Basolateral Export of Oxidized Fatty Acid Species

We next explored the utility of the platform for investigating small-molecule perturbations on fatty acid oxidation. Etomoxir, a carnitine palmitoyl transferase 1 (CPT1)

inhibitor, was used to inhibit fatty acid oxidation. When CPT1 is inhibited, fatty acids cannot be imported into the mitochondria where fatty acid oxidation normally catabolizes longer-chain fatty acids to smaller-chain fatty acids.[63] *CPT1A* is expressed robustly in primary human absorptive enterocytes both in vivo and in vitro on day 7 of

differentiation (Figure 5A). Etomoxir was used at a concentration of 100 umol/L because of recent reports[64–66] of off-target effects at high concentrations (>100 umol/L). After pretreatment with etomoxir, a variety of different-chain-length B–fatty acids (short-chain fatty acid, B-C5; medium-chain fatty acid, B-C12; or long-chain fatty acid, B-C16) were applied to the apical reservoir to mimic postprandial absorptive enterocyte exposure to fatty acids
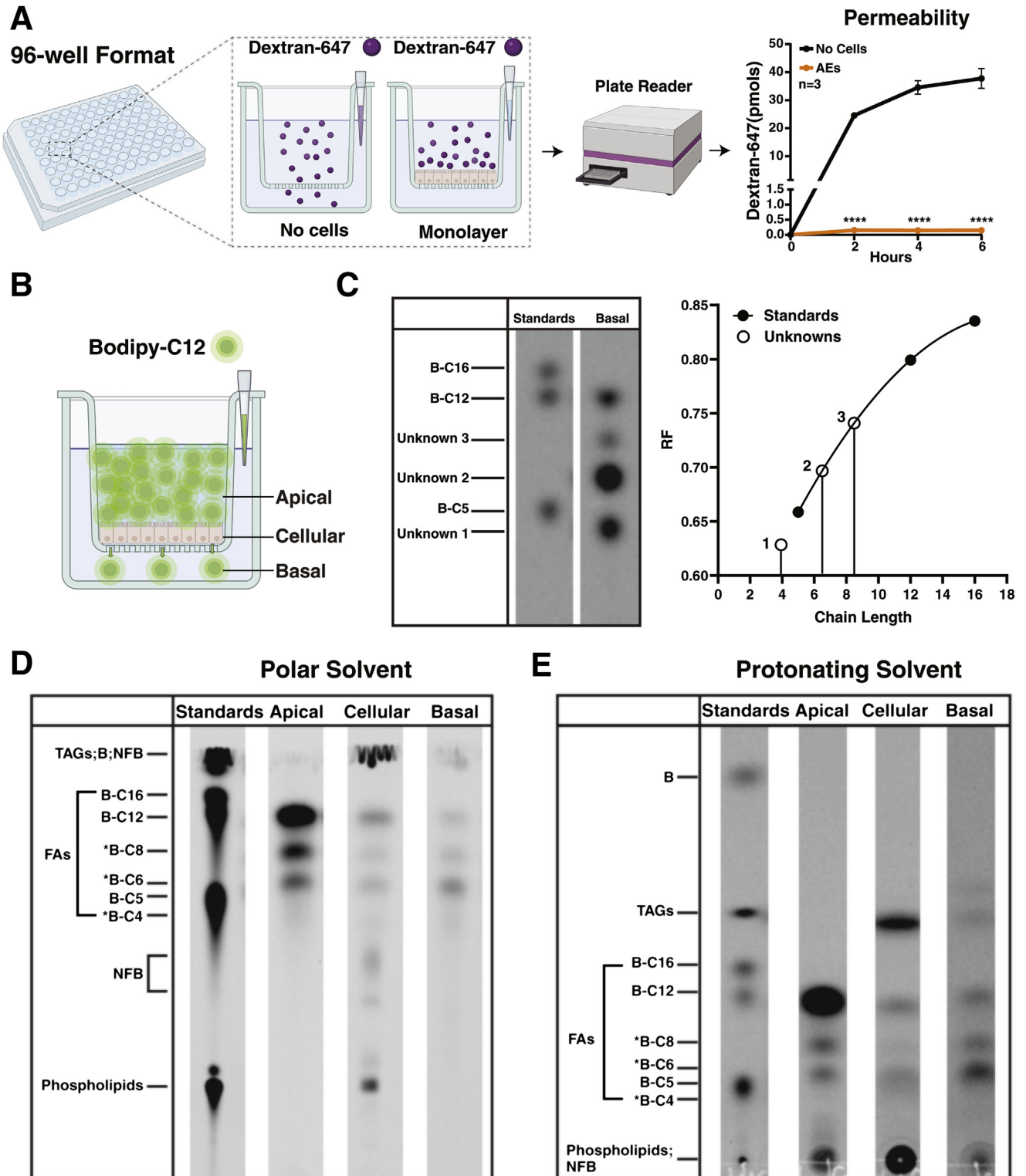
in vivo. Media from the basal reservoir was taken at 2, 4, and 6 hours after application of fluorescent fatty acids (Figure 7A). The impact of etomoxir on basal export of fatty acids and fatty acid metabolites was evaluated in real time by total fluorescence detection by plate reader, and TLC was used to identify BODIPY-labeled metabolites using small volumes of media from the 96-well Transwell platform (Figure 8A–C).

Strong barrier function through the duration of B–fatty acid and etomoxir treatment was confirmed by lack of Dextran-647 in the basal reservoir (Figure 7B). When B-C5 was the apical input fatty acid, basal fluorescence did not significantly change when fatty acid oxidation was inhibited (Figure 7A). By contrast, when B-C12 and B-C16 were the apical input fatty acids, fatty acid oxidation inhibition significantly reduced basal-reservoir fluorescence (Figure 7A). TLC showed that the most abundant lipid species in the basal reservoir of B-C5–treated cultures was B-C5 (Figure 8A), suggesting that this fatty acid diffused passively through absorptive enterocyte monolayers because fatty acids become increasingly water soluble as chain length decreases.[67] For control cultures (vehicle) treated with B-C12 and B-C16, the most predominant lipid species corresponded to B-C6 (Figure 8B and C), indicating catabolism of B-C12 and B-C16.

After treatment of B-C12 and B-C16 cultures with the fatty acid oxidation inhibitor etomoxir, B-C6 decreased significantly (Figure 8B and C). In B-C12–treated cultures, etomoxir caused the apical input fatty acid (B-C12) to be the predominant lipid species in the basal reservoir (Figure 8B). In cultures exposed to apical B-C16, etomoxir treatment did not result in B-C16 being the predominant lipid species in the basal reservoir (Figure 8C). These findings suggest that long-chain fatty acids (>B-C12) are less amenable to passive diffusion than short-chain (B-C5) and medium-chain (B-C12) fatty acids. Together these data indicate that fatty acids of shorter chain length (B-C5, B-C6) are more amenable to basal export by absorptive enterocytes than fatty acids of longer chain length (B-C12, B-C16), which appear to require catabolism via fatty acid oxidation to generate a shorter fatty acid derivative (B-C6) that then can be readily exported or diffuse to the basal reservoir.

Although total basal-reservoir fluorescence and TLC show that etomoxir reduces fatty acid export in B-C12 and B-C16 cultures, these results cannot rule out the possibility that etomoxir reduces basal-reservoir fluorescence by inhibiting apical fatty acid import, thus resulting in less intracellular fatty acid available to undergo fatty acid oxidation. To test whether etomoxir reduced apical fatty acid import, fluorescence from the apical reservoir of B-C12– and B-C16–treated cultures was quantified after 6 hours of etomoxir treatment (Figure 8F). If etomoxir reduced fatty acid import, there would be more total B–fatty acid fluorescence in the apical reservoir compared with control, however, the data showed the opposite, that etomoxir significantly reduced apical–reservoir fluorescence in cultures exposed to B-C12 and B-C16 (Figure 8F). These results support the conclusion that etomoxir does not reduce apical fatty acid uptake.

The finding that etomoxir significantly reduced both apical and basal reservoir fluorescence was somewhat surprising and raised the hypothesis that impaired fatty acid oxidation resulted in accumulation of B–fatty acids in the cellular reservoir. To test this, absorptive enterocyte monolayers were treated with B-C12 or B-C16 along with vehicle or etomoxir. After 6 hours of apical exposure, absorptive enterocyte monolayers were imaged to quantify cellular fluorescence (Figure 8D and E). Etomoxir significantly increased cellular reservoir fluorescence in B-C12/B-C16–treated cultures, further supporting the conclusion that impaired fatty acid oxidation reduced fatty acid export (Figure 8D and E). Together, these data support the conclusion that medium- and long-chain fatty acids are catabolized by fatty acid oxidation to smaller-chain fatty acids that can be exported as free fatty acids (Figure 8G).

Metformin and C75 Potentiate Fatty Acid Oxidation in Absorptive Enterocyte Monolayers and Increase Basolateral Export of Oxidized Fatty Acids

To further support a role for fatty acid oxidation in regulating basal export of B–fatty acids, it was hypothesized that treating absorptive enterocyte monolayers with drugs that augment fatty acid oxidation would result in increased fatty acid export. To test this hypothesis, absorptive enterocyte monolayers were treated independently with metformin and C75, drugs that show fatty acid oxidation

---

Figure 6. (*See previous page*). **Application of fluorescent polysaccharide and fatty acid show integral barrier and fatty acid handling in vitro.** (*A*) *Left*: Schematic showing application of Dextran-647 to the apical surface of absorptive enterocytes or empty Transwell cultures. *Right*: Subsequent sample collection and fluorescence quantification via plate reader. ISCs were differentiated for 7 days before application of 1 umol/L Dextran-647. A total of 50 uL media from the basal reservoir was removed at 2, 4, and 6 hours from empty Transwell inserts or absorptive enterocyte cultures and replaced with fresh differentiation media; Bonferroni multiple comparisons test. ****$P < .0001$. (*B*) Schematic of B-C12 application to absorptive enterocyte Transwell cultures and subsequent retrieval from apical, cellular, and basal reservoirs. (*C*) TLC (polar) of basal media from absorptive enterocyte cultures after 6 hours of incubation with B-C12 (*left*). Retention factor (RF) of B-C5, B-C12, and C16 standards were used to generate a standard curve to infer the chain length of fatty acids whose RF values do not correspond to B–fatty acid standards used (*right*). (*D* and *E*) TLC of apical, cellular, and basal reservoirs of absorptive enterocyte Transwell cultures after 6 hours of B-C12 application using polar and protonating solvents. A previous study[57] using TLC to identify B-lipid species with the same solvents used in this study reported NFBs that do not correspond to B-lipids used. *Location of B-C4, B-C6, and B-C8 were inferred from panel *C*. Experiments were performed in triplicate (n = 3 absorptive enterocyte Transwell cultures). AE, absorptive enterocyte; B, BODIPY; B-C4, B-C6, B-C8, B-C12, B-C16, BODIPY–fatty acids; FA, fatty acid; TAG, triglyceride.
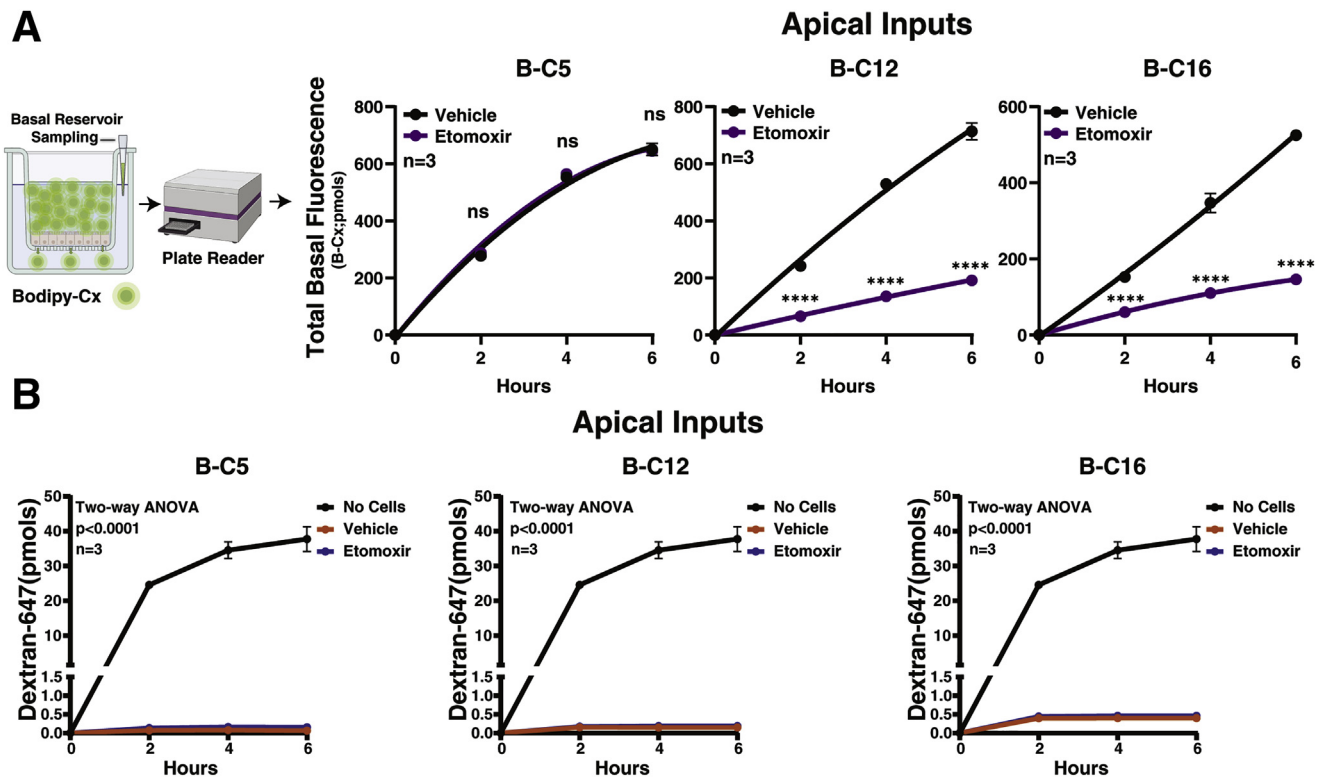
Figure 7. Etomoxir reduces fatty acid export. (*A*) *Left*: Schematic showing basal reservoir sampling after application of B–-fatty acids to the apical surface of absorptive enterocyte Transwell cultures and subsequent quantification of basal fluorescence via plate reader. *Right*: Quantification of basal fluorescence from B-C5–, B-C12–, and B-C16–treated absorptive enterocyte cultures treated with vehicle (dimethyl sulfoxide), or etomoxir. Bonferroni multiple comparisons test. ****$P < .0001$. A total of 50 uL basal media was collected and quantified by plate reader at 2, 4, and 6 hours after fatty acid application. (*B*) Quantification of Dextran-647 in the basal reservoir of absorptive enterocyte monolayers from basal samples of fatty acid–handling screens taken at 2, 4, and 6 hours. Bonferroni multiple comparison test. ****$P < .0001$. Experiments were performed in triplicate (n = 3 absorptive enterocyte Transwell cultures). ANOVA, analysis of variance; B-Cx, BODIPY lipids.

augmentation in other cell types.[68,69] Metformin, commonly known as an antidiabetic drug, potentiates fatty acid oxidation by preventing formation of the CPT1 inhibitor malonyl-CoA[70] and C75, a weight loss–inducing drug, potentiates fatty acid oxidation by increasing CPT1 activity[71] (Figure 9*F*). After metformin or C75 exposure, B-C12 or B-C16 was applied to the apical reservoir to mimic post-prandial fatty acid exposure. Media from the basal reservoir was collected at 2-hour intervals for 6 hours and total fluorescence was quantified to measure fatty acid export. Metformin and C75 significantly increased fluorescence in the basal reservoir of B-C12– and B-C16–treated monolayers (Figure 9*A*). Strong barrier function through the duration of B–fatty acid and agonist treatment was confirmed by lack of Dextran-647 in the basal reservoir (Figure 9*B*). TLC was performed to determine the lipid species exported to the basal reservoir of B-C12 and B-C16 cultures (Figure 9*C* and *D*). A lipid species corresponding to B-C6 was the most abundant B–fatty acid species in the basal reservoir of B-C12– and B-C16–treated cultures (Figure 9*C* and *D*), indicating that B-C6 is the primary B–fatty acid metabolite exported.

To probe whether the B–fatty acid export effects were dependent on fatty acid oxidation, absorptive enterocyte monolayers exposed to B-C12 or B-C16 were co-treated with each of the fatty acid oxidation potentiators, C75 or metformin, and the fatty acid oxidation inhibitor, etomoxir. After 6 hours of B–fatty acid exposure and drug treatment, basal reservoir fluorescence was quantified. Etomoxir blocked the ability of C75 and metformin to increase basal reservoir fluorescence in cultures exposed to B-C12 and B-C16 (Figure 9*E*), supporting the conclusion that metformin and C75 function in a fatty acid oxidation–dependent manner to increase basal export of oxidized long- and medium-chain fatty acid metabolites (Figure 9*F*).

Discussion

Once born from an ISC, progenitor cells transition through a number of lineage states during their 7-day lifespan in vivo.[72] Mouse studies suggest the absorptive lineage transitions through functional maturation states classified as early, intermediate, and mature phases as they migrate up the villus axis.[49] These functional maturation states are associated with different biological roles related to antimicrobial functions early on and progress into nutrient handling function toward their late and terminal maturation stage.[49] Here, we show by single-cell transcriptomics that
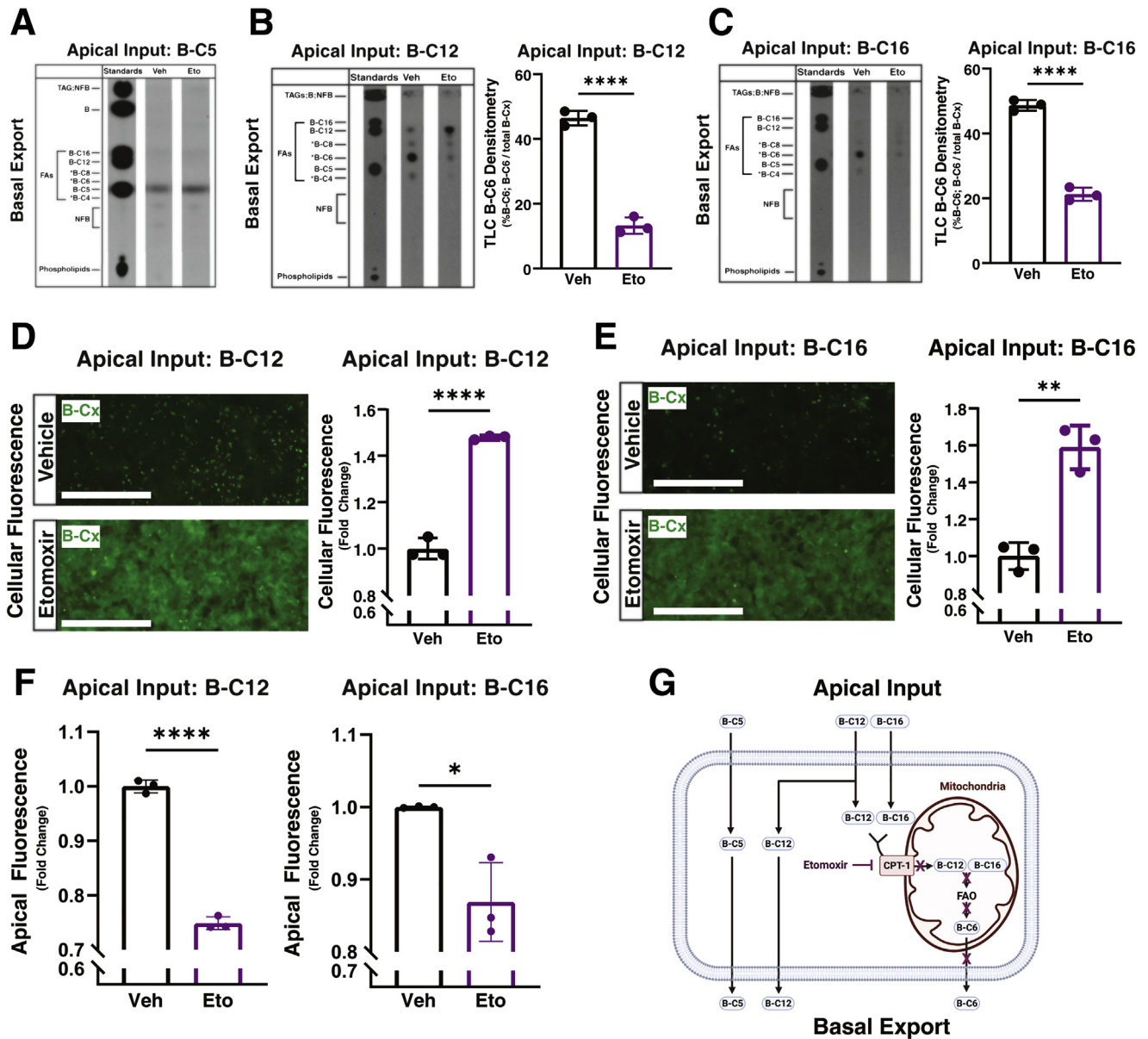
Figure 8. Inhibiting fatty acid oxidation reduces fatty acid export. (*A–C*) TLC of basal-reservoir media collected 6 hours after vehicle or etomoxir and B-C5, B-C12, or B-C16 application. A previous study[57] using TLC to identify B-lipid species with the same solvents used in this study reported NFBs that do not correspond to B-lipid standards used. Approximate locations of NFBs are labeled. *Location of B-C4, B-C6, and B-C8 were inferred from Figure 6*C*. (*B* and *C*) *Right*: Quantification of the fluorescence contributed by the B-C6 band divided by the cumulative fluorescence of all bands in each TLC lane. Unpaired *t* test. ****$P < .0001$. (*D* and *E*) Cellular-reservoir fluorescence of B-C12– or B-C16–treated absorptive enterocyte Transwell cultures treated with vehicle (dimethyl sulfoxide [DMSO]) or etomoxir. Unpaired *t* test. **$P < .01$, ****$P < .0001$. *Scale bars*: 100 um. (*F*) Apical-reservoir fluorescence of B-C12– or B-C16–treated absorptive enterocyte Transwell cultures treated with vehicle (DMSO) or etomoxir. Unpaired *t* test. *$P < .05$, ****$P < .0001$. (*G*) Schematic showing proposed mechanism of reduced B–fatty acid export by etomoxir. B-fatty acids were applied at a concentration of 20 umol/L. Etomoxir was applied at a concentration of 100 umol/L. Experiments were performed in triplicate (n = 3 absorptive enterocyte Transwell cultures). B-C$_x$, fluorescence coming from all B-lipids in basal, apical, or cellular reservoirs; Eto, etomoxir; FA, fatty acid; FAO, fatty acid oxidation; TAG, triglyceride; Veh, vehicle.

human jejunal absorptive enterocytes in vivo generally share a similar maturation defined by early, intermediate, and late maturation phases. Importantly, these states correlate with discrete lipid-handling gene profiles as absorptive enterocytes mature. Although our study focused on lipid-handling genes and mechanisms, the transcriptomic data sets will be useful to evaluate aspects of nutrient handling (ie, carbohydrate, protein, and vitamin metabolism) in primary human absorptive enterocytes.

The absorptive lineage is the default pathway taken by progenitor cells unless the master regulator of secretory lineage fate, Atoh1, is expressed.[54] Chromatin states across
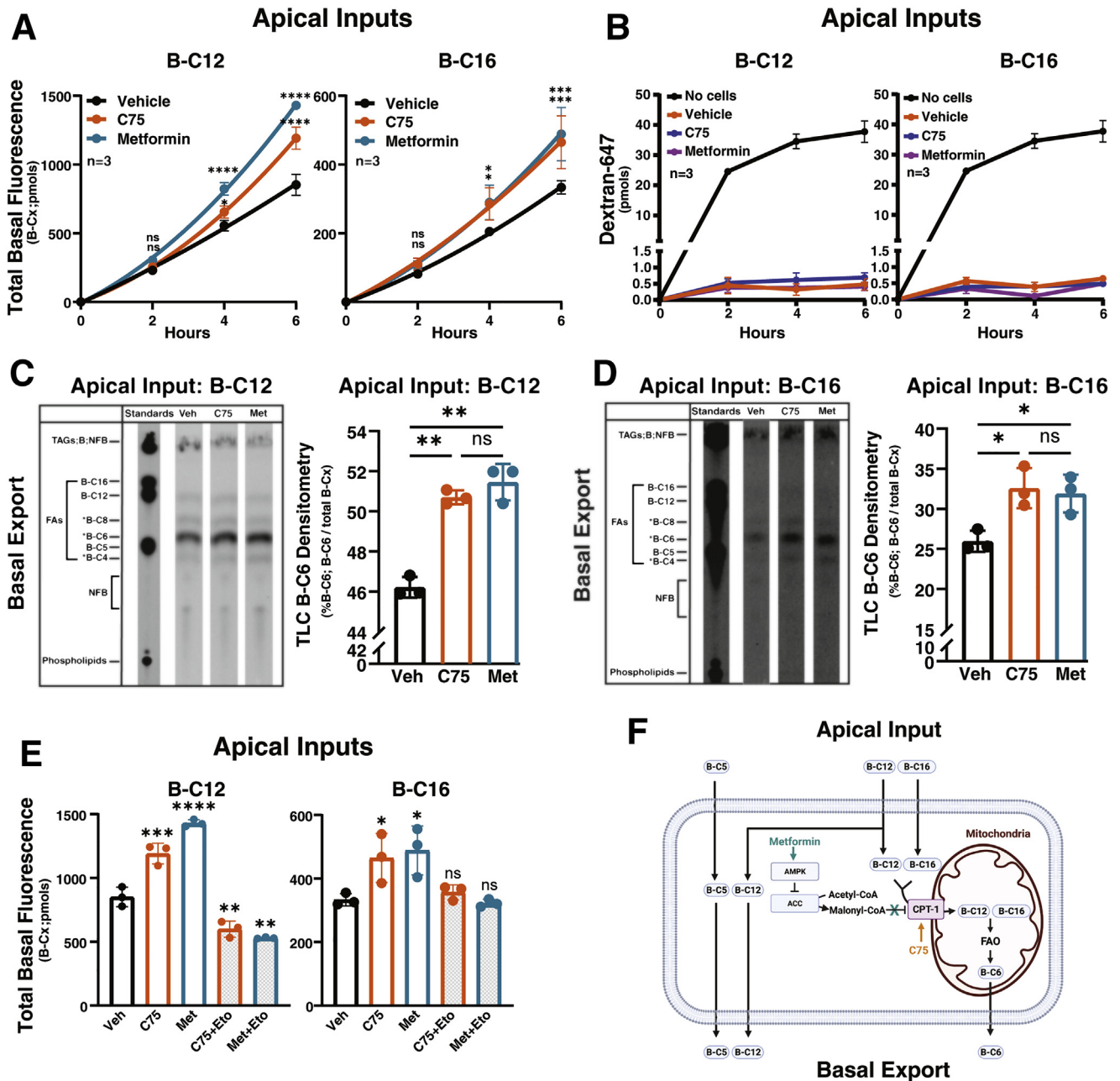
Figure 9. Enhancing fatty acid oxidation augments fatty acid export. (*A*) Quantification of basal-reservoir fluorescence from B-C12– or B-C16–treated absorptive enterocyte cultures treated with vehicle (dimethyl sulfoxide [DMSO]), C75, or metformin (Met). Bonferroni multiple comparisons test. *$P < .05$, ***$P < .001$, ****$P < .0001$. (*B*) Quantification of Dextran-647 in the basal reservoir of absorptive enterocyte monolayers from basal samples of fatty acid–handling screens taken at 2, 4, and 6 hours. Bonferroni multiple comparison test.****$P < .0001$. Experiments were performed in triplicate (n = 3 absorptive enterocyte Transwell cultures). (*C* and *D*) *Left*: TLC of basal-reservoir media from B-C12– or B-C16–treated absorptive enterocyte cultures treated with vehicle, C75, or metformin. *Right*: Quantification of the fluorescence contributed by the B-C6 band divided by the cumulative fluorescence of all bands in each TLC lane. Bonferroni multiple comparisons test. *$P < .05$, **$P < .01$. (*E*) Basal-reservoir fluorescence of B-C12–treated cultures treated with either vehicle, C75, metformin, C75 and etomoxir, or metformin and etomoxir. Fluorescence was measured 6 hours after B–fatty acid application. Bonferroni multiple comparisons test. *$P < .05$, **$P < .01$, ***$P < .001$, and ****$P < .0001$. (*F*) Proposed mechanism of enhanced fatty acid export by C75 and metformin. Concentrations of C75, metformin, and etomoxir were 40 umol/L, 3 mmol/L, and 100 umol/L, respectively. A previous study[57] using TLC to identify B-lipid species with the same solvents used in this study reported NFBs that do not correspond to B-lipid standards used. *Location of B-C4, B-C6, and B-C8 were inferred from the experiment in Figure 10. Experiments were performed in triplicate (n = 3 absorptive enterocyte Transwell cultures). ACC, acetyl-CoA carboxylase; AMPK, AMP-activated protein kinase; B-Cx, BODIPY-lipids; FA, fatty acids; FAO, fatty acid oxidation; Met, metformin; TAG, triglyceride; Veh, vehicle.

the genome are associated with hardwiring of some lineage-specification programs,[73,74] and dynamic chromatin states have been described as cells move through ISC to secretory and absorptive lineage states.[73,74] Data presented here show that removal of ISC maintenance factors from ISC monolayers promote a stereotypical absorptive enterocyte lineage program in an epithelial-autonomous manner, suggesting human absorptive enterocytes are hardwired to undergo progressive maturation over time. Because our in vitro absorptive enterocyte monolayer system generally mimics in vivo absorptive enterocyte maturation and life-span, it is highly suited to define the intrinsic nature of chromatin dynamics through human absorptive enterocyte maturation and is amenable to testing how extrinsic influences such as dietary factors or the microbiome might influence chromatin states and associated gene expression.

The majority of dietary lipids consist of long-chain fatty acids. Long-chain fatty acids undergo intracellular esterification to triglycerides, are packaged into chylomicrons, exported through the basal membrane, and distributed through the lymphatic system.[1,2] Previous studies have shown that short-chain fatty acids and medium-chain fatty acids can bypass the chylomicron-lymphatic pathway and pass unesterified into the portal vein.[75] Because long-chain fatty acids can be oxidized to short-chain fatty acids and medium-chain fatty acids via fatty acid oxidation, we hypothesized that fatty acids derived from fatty acid oxidation of long-chain fatty acids could be exported through the basal membrane as free fatty acids. Using our culture system, we show that smaller-chain fatty acids generated from fatty acid oxidation of long-chain fatty acids can be exported unesterified across the basal membrane of absorptive enterocytes. We show a dependency on fatty acid oxidation in regulating basal export of long-chain fatty acid–derived fatty acids because their basal export was decreased by inhibiting fatty acid oxidation with etomoxir and increased by enhancing fatty acid oxidation with C75 and metformin. This novel pathway of long-chain fatty acid–derived fatty acid export might explain why patients with abetalipoproteinemia show distribution of the majority of dietary fatty acids yet are unable to secrete chylomicrons.[76]

Basal export of free fatty acids regulated by fatty acid oxidation could be involved in other physiological responses to dietary lipids, disease etiologies, and pharmaceuticals that target fatty acid oxidation pathways. Our findings show that metformin, a satiety-inducing/glucose-lowering drug, enhances basal fatty acid export. Stimulation of free fatty acid receptors, which are restricted to the basal surface[77] of enteroendocrine cells[71] immediately adjacent to absorptive enterocytes, stimulate secretion of glucose-lowering glucagon-like peptide 1 (GLP-1) and satiety-inducing peptide YY (PYY)[78] gut hormones. Reports have shown that metformin elicits intestinal GLP-1 secretion by enteroendocrine cells and that this effect significantly contributes to systemic glucose lowering.[79] This raises the possibility that the absorptive enterocyte–enteroendocrine cell axis uses fatty acid oxidation to augment basal fatty acid export, which may be a mechanism underlying some of the efficacy of metformin.

Importantly, exposure of metformin to immortalized enteroendocrine cell lines fails to stimulate GLP-1 secretion, suggesting metformin does not act directly on enteroendocrine cells to stimulate GLP-1 secretion but rather through a more complex mechanism.[80] In light of our results showing metformin increases fatty acid export, metformin may act to increase GLP-1 secretion via an absorptive enterocyte–fatty acid oxidation–enteroendocrine cell axis. In this scenario, apically localized medium-chain fatty acids and long-chain fatty acids are absorbed by absorptive enterocytes, catabolized to shorter-chain fatty acid species that can passively diffuse through the basolateral membrane, where they interact with nearby free fatty acid receptors on enteroendocrine cells to stimulate GLP-1 release. Further development of our absorptive enterocyte culture system to support co-culture of enteroendocrine cell and absorptive enterocytes with loss and gain of function for key fatty acid oxidation genes will be required to test this hypothesis.

Aside from basic science applications, our high-throughput, 96-well, absorptive enterocyte culture platform is highly suitable for drug screening and validation. Compared with standard 12-well Transwell plates, scaling the platform to 96-wells increases the plate form factor by 8 while simultaneously requiring approximately 8 times fewer cells. This substantially increases the number of biological and technical replicates that can be performed per plate and reduces plate-to-plate variability when performing experiments to evaluate therapeutic indices for a drug. Real-time quantification of fatty acid mobilization through the epithelial barrier by plate reader allows for kinetic studies, while the planar format of these cultures facilitates simultaneous high-content microscopic readouts. Although the absorptive enterocyte monolayer surface and reservoir sample volumes are small, we show that sufficient material for RNA sequencing and highly sensitive detection of B-conjugated fatty acids and metabolites by plate reader and TLC remains. The scalability, physiological relevance, and sensitivity of our platform to detect changes in fatty acid handling could facilitate the discovery of treatments for metabolic disorders impacted by intestinal fatty acid handling such as obesity, dyslipidemia, and diabetes.

Materials and Methods
Donor Selection

Human donor intestines were accepted and received from HonorBridge (formerly Carolina Donor Services, Durham, NC) based on the following donor acceptance criteria: age 65 years or younger; brain-dead only (as opposed to donation after cardiac death); and negative for human immunodeficiency virus, hepatitis, rapid plasma region (RPR) test for syphilis, tuberculosis, or Coronavirus Disease 2019. Tissue from a 29-year-old Caucasian man was used for single-cell dissociation and scRNAseq. Tissue from a 51-year-old African American man was used for tissue culture, in situ hybridization, scRNAseq of collagen-grown ISCs and absorptive enterocyte monolayers, and bulk RNAseq. Human donors had no history of bowel surgery, severe abdominal injury, cancer, or chemotherapy.

Increased-risk donors (ie, history of incarceration or intravenous drug use) were accepted, provided negative infectious disease results were obtained. In addition, donor cases in which the pancreas was placed for transplant were excluded given that pancreatic transplants require removal of proximal small intestinal tissue.

Organ Resection and Single-Cell Dissociation

Whole human intestines were transported to University of North Carolina Chapel Hill in ice-cold University of Wisconsin Solution, with tissue dissection beginning within 8 hours of cross-clamping. First, fat and connective tissue were trimmed from the donated organs and intestines were subdivided into 6 regions after measurement. For the small intestine, the proximal 20 cm was deemed duodenum. Jejunum and ileum were determined through an even split of the remaining small intestine. Two 3×3 cm^2 resections were isolated from the center of jejunum and ileum for dissociation.

Resections were incubated in 10 mmol/L N-acetyl-cysteine at room temperature for 30 minutes to remove mucus, then tissue was moved to ice-cold isolation buffer, which consisted of 5.6 mmol/L Na2HPO4, 8.0 mmol/L KH2PO4, 96.2 mmol/L NaCl, 1.6 mmol/L KCl, 43.4 mmol/L sucrose, 54.9 mmol/L D-sorbitol, and 100 umol/L Y27632, and then washed several times by gently inverting the tubes. Tissues then were incubated in Isolation Buffer with 2 mmol/L EDTA and 0.5 mmol/L dithiothreitol, and then shaken vigorously to remove crypts. Shakes were repeated several times, checking for crypts and/or villi each time. High-yield small intestinal shakes were pooled to approximate 1:1 villus-to-crypt tissue by cell mass. Crypts and villi were dissociated to single cells using 4 mg/mL protease VIII in Dulbecco's phosphate-buffered saline (DPBS) + Y27632 on ice for approximately 45 minutes with trituration via a P1000 micropipette every 10 minutes. Dissociation was checked on a light microscope and then clumps were removed using filtration.

Cell Sorting, Library Preparation, and Sequencing

Single cells were washed with DPBS + Y27632 and then resuspended in Advanced Dulbecco's modified Eagle medium (DMEM)/F12 + 1% bovine serum albumin + Y-27632. Annexin V-Allophycoallenine (APC) (1:100) was added for live/dead staining and 1 TotalSeq Anti-Human Hashtag Antibody (Biolegend, San Diego, CA) per region to allow for tracking all 6 regions with a single library preparation. Cells were washed with Advanced DMEM/F12 + 1% bovine serum albumin + Y27632 and then resuspended in the same solution for sorting on a Sony Cell Sorter SH800Z (Sony, Tokyo, Japan). Cells were gated using forward and backward scatter and Annexin V to enrich for live single epithelial cells (Figure 10A–E). Annexin V staining showed high viability (95.7%) of single cells, with 1788 having passed quality filtering (Figure 10E). Twenty-five thousand cells were collected from each separate region, and then all regions were combined before sequencing. Library preparation was performed with the Chromium Next GEM Single Cell 3' GEM, Library & Gel Bead Kit v3.1 (10×

Genomics, Pleasanton, CA). Sequencing was performed on an Illumina NextSeq 500 (Illumina, San Diego, CA).

scRNAseq Data Processing

After sequencing, reads were aligned to reference transcriptome GRCh38 with the 10× Cell Ranger pipeline (10× Genomics, Pleasanton, CA). Mapped reads were filtered and counted by barcode and Unique Molecular Identifier (UMI) and then transformed into an AnnData object using the Python (Beaverton, OR) implementation of scanpy (v1.7.2). Annotations for cell-cycle phase were added after previously published methods.[81] The number of genes, number of UMIs, and percentage of mitochondrial expression for all cells in each sample were visualized and used to identify thresholds for high-quality cells to include in further analysis (Figure 10F and G, Table 2).[82] After filtering, read counts were log-transformed and normalized to the median read depth of the data set. For both single-cell sequencing experiments no batch correction was performed because each data set was analyzed separately. Variability owing to read count, percentage of mitochondrial reads, and cell-cycle phase were regressed out by simple linear regression. Highly variably genes were identified using Seurat (New York, NY).[83] A total of 2585 and 4186 highly variable genes were used for principal component analysis for the in vivo and in vitro scRNAseq data sets, respectively. Counts for each gene were scaled to have a mean of zero and unit variance. A k-nearest neighbor (kNN) graph was constructed with 10 neighbors and was used to calculate Leiden clusters for both in vivo and in vitro scRNAseq data sets (in vivo clustering parameters: Leiden resolution = 0.5, num_neighbors = 10, num_pcs = 40; in vitro clustering parameters: Leiden resolution = 0.1, num_neighbors = 10, num_pcs = 15) and Epithelial Cell Adhesion Molecule-negative (EPCAM-) cells were removed from the in vivo data set.[43] PAGA (Munich, Germany) was used to initialize UMAP (Ottawa, Ontario) embeddings of Leiden clusters.[84,85]

Regional hashtag deconvolution followed published methods for both scRNAseq data sets. Briefly, raw hashtag read counts were normalized using centered log ratio transformation followed by k-medoid clustering (k = 6 medoids). Hashtag noise distributions were determined by removing the cluster with the highest expression of a specific hashtag, then a negative binomial distribution was fit to the data of the remaining cells. Cells were considered positive for a hashtag if counts for the specific hashtag were greater than the distribution's 99th percentile ($P < .01$) threshold. Cells positive for multiple hashtags were excluded as likely doublets. Cells called for colon and duodenum were removed from the data set. For in vitro data, only hashtags 1 and 3 were kept for analysis.

RNA Velocity

Velocyto (Cambridge, MA) 0.17.16 was used to generate the initial loom file and scvelo (Munich, Germany) 0.2.4 was used for all integration of spliced/unspliced loom file integrations with the processed anndata (Munich, Germany) object and all subsequent trajectory analysis.[50,51,86] Briefly,
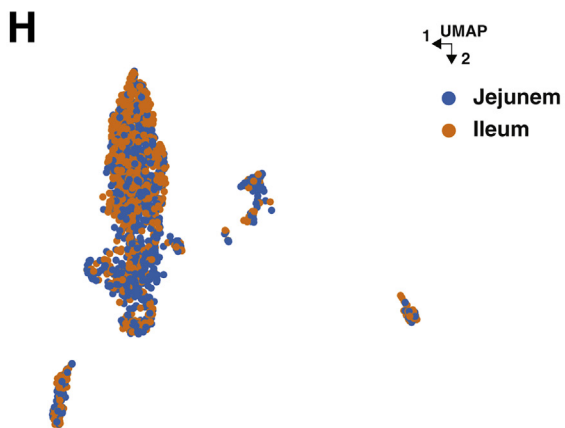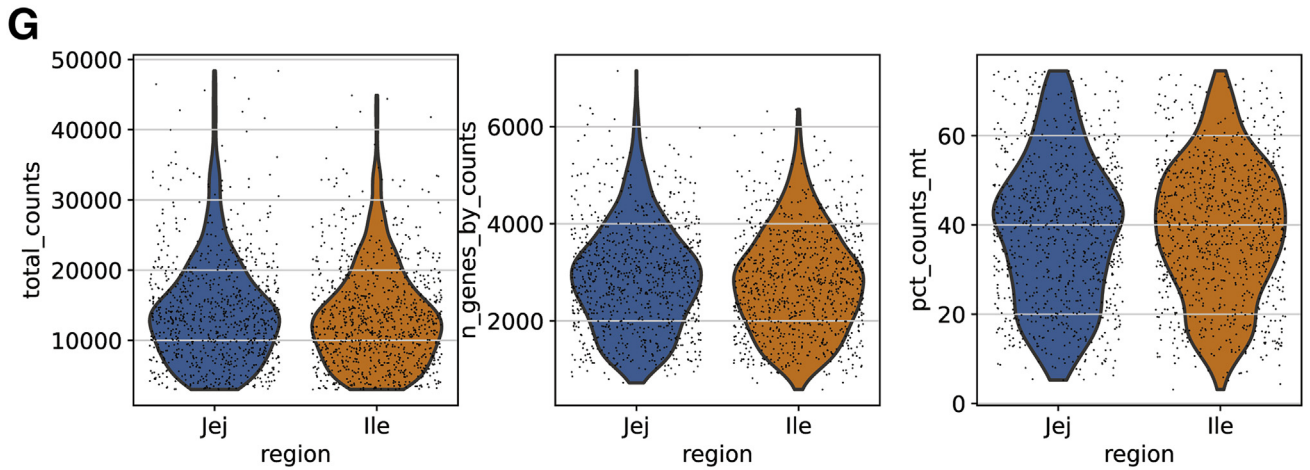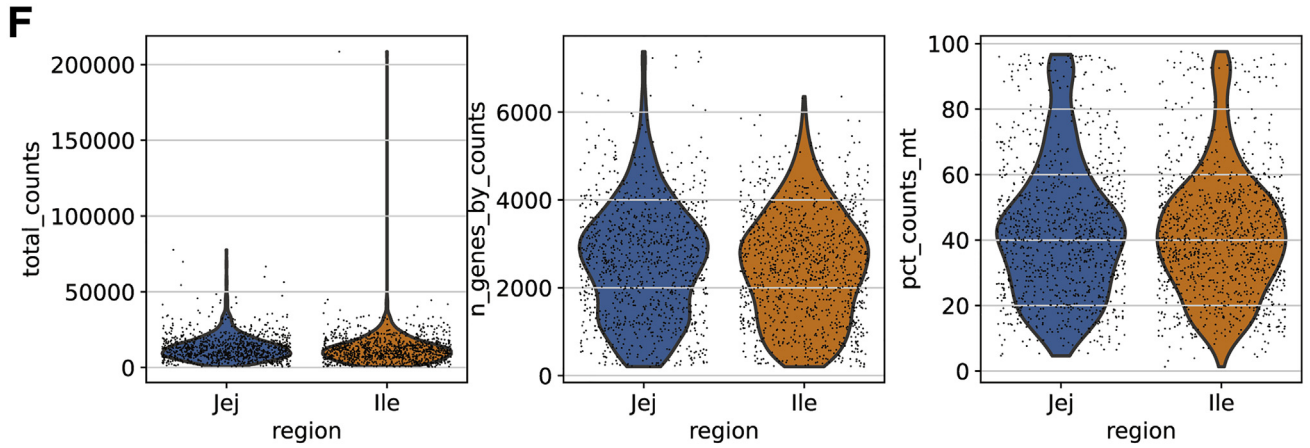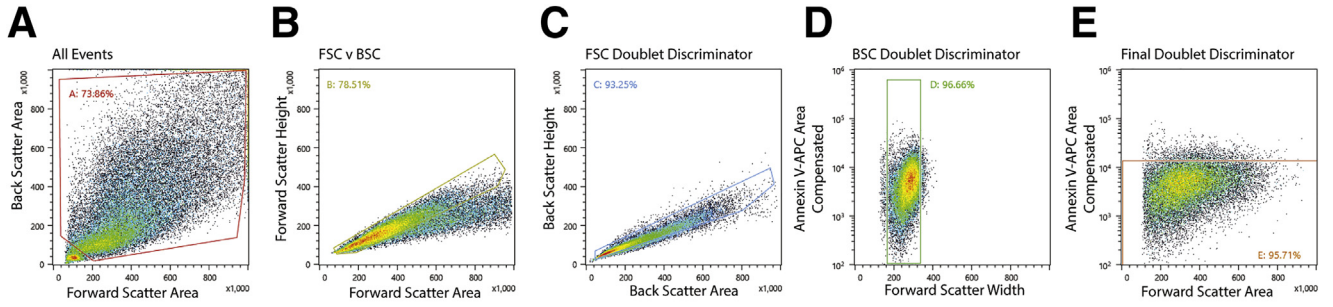
Table 2. Quality Control Parameters for scRNAseq

	In vivo scRNAseq	In vitro scRNAseq
Minimum genes	>500	>1000
Percentage of mitochondrial reads	<75%	<50%
Minimum counts	>3000	>5000
Maximum counts	<50,000	<80,000

to ensure connectedness of the data set, clusters that corresponded to stem cells and the different stages of enterocyte differentiation were used for trajectory analysis. All other clusters were removed from the data set and the remaining clusters were reprocessed and reclustered. The resulting data set was integrated with the spliced and unspliced read counts and 4100 highly variable genes were kept for fitting to the RNA velocity dynamic model. For moment calculation, num_pcs = 40 and num_neighbors = 50. Function arguments for calculating RNA velocity vectors and latent time were default values, except for the specification of the dynamic model in scvelo.tl.velocity.

Differential Gene Expression for scRNAseq

Differential expression analysis was performed using the de.test.wald function in the Python implementation of diffxpy (version 0.7.4).[87] From the output data, significant DEGs ($q < .05$) were attributed to the cluster with the highest mean value for each gene.

Linear Correlation Analysis

Read count data from both data sets were normalized to the same value and then log-transformed. The mean expression values for each lipid-handling gene were calculated per scRNAseq cluster and per group of in vitro differentiation bulk RNAseq. Pairwise comparisons of mean gene expression values for each in vivo differentiation state and each in vitro differentiation state were made (Figure 5B). A line was drawn representing a perfect correlation of in vitro bulk RNAseq expression to in vivo scRNAseq expression (Figure 5B). Residuals for each lipid-handling gene were calculated based on the deviation from this line. The residual sum of squares thus represents a quantitative measure of the overall similarity of expression of lipid-handling genes between each in vivo differentiation state and each in vitro differentiation state, with a lower value indicating a better fit to the line describing a perfect correlation.

2D Collagen Scaffold Preparation

2D collagen scaffolds were made by diluting ice-cold type I rat tail collagen (354236; Corning, Corning, NY) to 1 mg/mL in ice-cold neutralization buffer according to an established protocol.[37] Briefly, 6-well tissue-culture plates (3516; Corning) were incubated at 37°C for 1 hour before 1 mL diluted rat-tail collagen was poured into each well. After collagen was poured into each well of a 6-well plate, plates were tilted to completely coat the bottom of each well. Plates then were incubated at 37°C for 1 hour before being overlaid with 3 mL room-temperature DPBS. Collagen scaffolds were kept overlaid with DPBS at room temperature until seeded with ISCs.

2D Collagen ISC Culture and Passaging

Primary human jejunal crypts of Lieberkühn were isolated and cultured on 2D collagen scaffolds according to an established protocol.[37] Briefly, after isolation, crypts were suspended in expansion media (EM) with 10 mmol/L Y27632 at a density of approximately 1667 crypts/mL. DPBS was removed from 6-well collagen-coated plates and immediately seeded with 3 mL suspended crypts. Media was removed the following day and replaced with fresh EM without Y27632. Media was changed every other day.

Six-well collagen ISC cultures were passaged when they became approximately 70% confluent according to an established protocol.[37] Briefly, ISCs containing collagen scaffolds were detached from the tissue culture plate by applying a 1-mL pipette tip to the side of the well and moving the tip around the entire perimeter. Once the collagen scaffold detached from the well, it was transferred to a 5-mL canonical using a 1-mL pipette. Next, 1 mL EM and 10 mmol/L Y27632 were added to the 5-mL conical containing the collagen scaffold and ISCs. To digest the collagen scaffold, 100 uL collagenase type IV was added to the conical and incubated at 37°C for 10 minutes. Once the collagen was dissolved, ISCs were pelleted at 800 × g for 3 minutes. The supernatant was removed and ISCs were resuspended in 5 mL DPBS. ISCs were pelleted and supernatant was removed as before. To dissociate ISC monolayers, ISCs were resuspended in 150 uL TrypLE Express (Thermo Fisher Scientific, Waltham, MA) containing 10 mmol/L Y27632 and incubated at 37°C for 5 minutes. After incubation, ISC monolayers were triturated by pipetting up and down 10 times against the bottom of the tube with a 1-mL pipette. Note that ISC monolayers were not dissociated to single cells. After trituration, ISCs were pelleted, and supernatant was aspirated as before. ISCs were resuspended in 9 mL EM with 10 mmol/L Y27632 and seeded in

---

Figure 10. (*See previous page*). **(A–E) Fluorescence-activated cell sorter (FACS) density plots showing FACS gating strategy for sorting live cells from dissociated human small intestine.** Titles above plots indicate the gate from where the cells came (ie, the previous density plot). (A) Initial doublet discriminator, with exclusion of likely red blood cells and immune cells. (B) Forward-scatter–based doublet discriminator. (C) Back-scatter–only doublet discriminator. (D) Forward-scatter width-based doublet discriminator. (E) Final gate used to distinguish live cells based on negative gating for Annexin V-APC. (F and G) Violin plots showing distributions of quality control (QC) parameters including the number of total reads per cell, number of genes counted in each cell, and the percentage of mitochondrial reads per cell. (F) Prefiltering distribution of QC parameters. (G) Postfiltering distribution of QC parameters. (H) Region of cells overlaid on UMAP. BSC, backscatter; FSC, forward scatter; Jej, jejunum; Ile, ileum; UMAP, uniform manifold approximation and projection.

three 6-well collagen scaffolds at 3 mL/well. Passaging was performed until the desired number of cells was obtained.

Transwell Preparation, ISC Seeding, Expansion, and Differentiation

Transwells were prepared according to an established protocol.[37] Briefly, the apical surface of 12-well (3460; Corning) or 96-well (7369; Corning) Transwell inserts was overlaid with ice-cold 1% Growth Factor Reduced Matrigel (Corning, Corning, NY) diluted in ice-cold DPBS. Transwell plates were left incubating at 37ºC in 5% CO_2 overnight. Inserts were rinsed by replacing the 1% Matrigel with DPBS the following day. After Transwell preparation, 2D collagen ISC monolayers were dissociated as previously described and ISCs were suspended in EM containing 10 mmol/L Y27632 at approximately 280,000 cells/mL. Suspended ISCs were seeded on the apical surface of Transwell inserts (500 uL for 12-well Transwells, 150 uL for 96-well Transwells). EM was added to the basal reservoir at the time of seeding (1.5 mL for 12-well Transwells, 240 uL for 96-well Transwells). Apical and basal media was replaced the day after seeding with fresh EM without Y27632. To induce differentiation, EM in apical and basal reservoirs was replaced with DM to initiate differentiation.

Adapting 2D Transwell Cultures for 96-Well Transwell Plates

For scaling to 96-well Transwell cultures, 25 mL media reservoirs and a 12-channel pipette were used for transferring 1% Matrigel, DPBS, and media to 96-well Transwell plates. Ninety-six–well Transwell inserts were covered with a hydrophobic porous film (12-631; Genesee Scientific, San Diego, CA) to minimize well-to-well variability caused by evaporation while maintaining gas exchange. For inducing differentiation in 96-well Transwell cultures, EM in the apical and basal surface was replaced with DM (apical, 100 uL; basal, 240 uL).

Single-Cell Dissociation of Transwell Epithelial Monolayers

Media was removed from ISCs expanded on collagen and from absorptive enterocytes on 12-well Transwell inserts and washed with 1× DPBS. A total of 1.5 mL of 3 mmol/L EDTA in phosphate-buffered saline was applied to ISCs expanded on collagen and on apical and basal reservoirs of 12-well Transwell cultures until most cells were lifted off the collagen or Transwell surface as determined by visual inspection every 2 minutes under an inverted microscope. EDTA was aspirated using a P1000 micropipette and redistributed over the Transwell surface to facilitate detachment of cells from the Transwell at 2-minute intervals until the majority of cells had detached. After the cells detached, 1.5 mL DPBS was applied to each well and rinsed by aspirating and re-applying the EDTA/DPBS. Cells then were aspirated and pelleted by centrifugation at 500 × g for 5 minutes. The supernatant was removed and replaced with 1 mL of 4 mg/mL cold protease in DPBS. Cells in cold protease were incubated on ice and pipetted semivigorously 10 times every 2 minutes before visual examination of dissociation under an inverted light microscope. This was repeated until all cells were singlets. After single-cell dissociation, the cold protease was quenched with Advanced DMEM/F12 + 1% fetal bovine serum. Cells were pelleted as described earlier and resuspended in Advanced DMEM/F12 + 1% fetal bovine serum.

Bulk RNA Sequencing Preparation, Processing, and Analysis

To investigate the dynamic changes in gene expression as ISCs differentiate into absorptive enterocytes in vitro, RNAseq was performed on human intestinal epithelial monolayers immediately before seeding onto Transwells (day 0) and on days 2, 5, 7, 10, and 11 of differentiation on Transwells. Three samples were collected from each time point and RNA was extracted using the RNAqueous-Micro Total RNA Isolation Kit according to the manufacturer's protocols and stored at −80°C. RNA quality was assessed before library preparation by using the Agilent 2100 Bioanalyzer (Agilent Technologies, Santa Clara, CA) to determine the RNA integrity number.[88] After confirmation that each sample had an RNA integrity number of at least 8, integrated fluidic circuits for gene expression and genotyping analysis were prepared using the Advanta RNA-Seq NGS Library Prep Kit (Fluidigm, South San Francisco, CA) for the Fluidigm Juno and sequenced with the Fluidigm Biomark HD system. Gene level expression was obtained through pseudo-alignment of reads to human genome GRCh38 using Kallisto (Berkeley, CA).[89] Expression values for plotting were obtained by Trimmed Mean of M-values (TMM) normalization across all samples using EdgeR (Parkville, Australia) package.[90,91] Sequencing data from each time point were combined and then normalized to the data set median and log transformed. Principal component analysis was performed with scikitlearn (v0.24.0, Rocquencourt, France).[92]

TEER

Barrier integrity of 96-well Transwell cultures was monitored by quantifying TEER using EVOM or EVOM3 (World Precision Instruments, Sarasota, FL) TEER meters in conjunction with STX100C96 electrodes (World Precision Instruments).

Basal Fluorescence Quantification

Etomoxir (100 umol/L), 40 umol/L C75, 3 mmol/L metformin, or vehicle (dimethyl sulfoxide) were suspended in 100 uL DM and applied to the apical surface of absorptive enterocyte Transwell cultures for 1 hour. After incubation, apical media was replaced with 100 uL DM containing drugs or vehicle, 1 umol/L dextran, Alexa Fluor 647 (Dextran-647), and 20 umol/L of either BODIPY-FL C5, BODIPY-FL C12, or BODIPY-FL C16 (Figures 7B and 9B). Basal media (50 uL) was collected at 2, 4, and 6 hours and replaced with an equivalent volume of DM. Quantification of basal

Table 3. Reagents Used

Reagents	Company	Catalog number
L-WRN cells	ATCC (Manassas, VA)	CRL-3276
Advanced DMEM/F12	Thermo Fisher (Waltham, MA)	12634010
Glutamax, 100×	Thermo Fisher (Waltham, MA)	35050061
1 mol/L HEPES buffer	Corning (Corning, NY)	25-060-CI
Primocin	VWR (Radnor, PA)	MSPP-ANTPM2
N-acetyl-cysteine	MilliporeSigma (Burlington, MA)	A9165
EGF, murine	Peprotech (Rocky Hill, NJ)	315-09
Nicotinamide	MilliporeSigma (Burlington, MA)	N0636-100G
B27	Thermo Fisher (Waltham, MA)	12587-010
Gastrin	MilliporeSigma (Burlington, MA)	G9145-1MG
PGE2	Peprotech (Rocky Hill, NJ)	3632464
A 83-01	MilliporeSigma (Burlington, MA)	SML0788-5MG
SB202190	Peprotech (Rocky Hill, NJ)	1523072
DPBS	Thermo Fisher (Waltham, MA)	14190-144
Matrigel	Corning (Corning, NY)	354230
Y27632	Selleckchem (Houston, TX)	S6390
Etomoxir	MilliporeSigma (Burlington, MA)	E1905-5MG
C75	Cayman Chemical (Ann Arbor, MI)	10005270
Metformin	Cayman Chemical (Ann Arbor, MI)	13118
Dimethyl sulfoxide	MilliporeSigma (Burlington, MA)	D2650-5X5ML
Glyoxal solution 40 wt % in H_2O	MilliporeSigma (Burlington, MA)	128465
TrypLE Express	Thermo Fisher (Waltham, MA)	12605010
Dextran 647	Thermo Fisher (Waltham, MA)	D22914
a-BODIPY 530/550-C12-HPC	Thermo Fisher (Waltham, MA)	D3792
BODIPY FL C16	Thermo Fisher (Waltham, MA)	D-3821
BODIPY FL C12	Thermo Fisher (Waltham, MA)	D-3822
BODIPY-FL C5	Thermo Fisher (Waltham, MA)	D-3834
BODIPY 493/503	Thermo Fisher (Waltham, MA)	D-3922
18:1-18:1-C11 TopFluor TG	Avanti Polar Lipids (Birmingham, AL)	810298C-1mg
Na_2HPO_4	MilliporeSigma (Burlington, MA)	S7907
KH_2PO_4	MilliporeSigma (Burlington, MA)	P5655
NaCl	MilliporeSigma (Burlington, MA)	S5886
KCl	MilliporeSigma (Burlington, MA)	P5405
Sucrose	Thermo Fisher (Waltham, MA)	BP 220-1
D-sorbitol	Thermo Fisher (Waltham, MA)	BP439-500
EDTA	Corning (Corning, NY)	46-034-CI
DTT	Thermo Fisher (Waltham, MA)	BP172-5
Protease VIII	MilliporeSigma (Burlington, MA)	P5380
Bovine serum albumin	Thermo Fisher (Waltham, MA)	BP1600-1
TotalSeq-B0251 anti-human hashtag 1 antibody	BioLegend (San Diego, CA)	394631
TotalSeq-B0251 anti-human hashtag 2 antibody	BioLegend (San Diego, CA)	394633
TotalSeq-B0251 anti-human hashtag 3 sntibody	BioLegend (San Diego, CA)	394635
TotalSeq-B0251 anti-human hashtag 4 antibody	BioLegend (San Diego, CA)	394637
TotalSeq-B0251 anti-human hashtag 5 antibody	BioLegend (San Diego, CA)	394639
TotalSeq-B0251 anti-human hashtag 6 antibody	BioLegend (San Diego, CA)	394641
Annexin V-APC	BioLegend (San Diego, CA)	640920
RNAqueous-Micro Total RNA Isolation Kit	Thermo Fisher (Waltham, MA)	AM1931
Chromium Next GE M Single-Cell 3' GEM, Library and Gel Bead Kit v3.1	10x Genomics (Pleasanton, CA)	PN-100012
RNAscope Probe - Hs-FABP1-C3	Advanced Cell Diagnostics (Newark, CA)	534801-C3
RNAscope Probe - Hs-APOA4	Advanced Cell Diagnostics (Newark, CA)	857841
RNAscope Probe - Hs-OLFM4-C2	Advanced Cell Diagnostics (Newark, CA)	311041-C2
RNAscope Probe - Hs-DMBT1	Advanced Cell Diagnostics (Newark, CA)	478711

DTT, dithiothreitol; EGF, epidermal growth factor; HPC, 1-Hexadecanoyl-*sn*-Glycero-3-Phosphocholine L-WRN, L-cell derived Wnt3a, R spondin 3, and Noggin; PGE2, prostaaglandin E2.

fluorescence was performed using a CLARIOstar Plus Microplate Reader (BMG Labtech Inc., Ortenburg, Germany). Fluorescence arbitrary units were converted to picomoles using a standard curve.

TLC

For the assessment of fatty acid handling via TLC (Figure 4), BODIPY-FL C12 was applied to the apical surface of absorptive enterocyte Transwell cultures. Apical and basal media were collected after 6 hours. Cells were released from Transwell inserts via application of 100 uL 1× TrypLE Express containing 10 mmol/L Y27632. Cells were lysed by undergoing 3 freeze-thaw cycles. Lipid extracts were generated from apical and basal media along with cell lysates using the Bligh and Dyer method.[93] Lipid extracts were resuspended in 100% ethanol and spotted on silica gel TLC plates. Lipid species were separated by placing spotted silica gel plates in a glass chamber containing either a polar (chloroform/ethanol/triethylamine/water, 30:34:30:8 mL) or protonating (petroleum ether/ethyl ether/acetic acid, 45:5:0.5 mL) solvent.

The following BODIPY analogs were used as standards to identify lipid species: BODIPY-FL C5 (B-C5), BODIPY-FL C12 (B-C12), BODIPY-FL C16 (B-C16), BODIPY 493/503 (B), and β-BODIPY-FL C12-1-Hexadecanoyl-sn-Glycero-3-Phosphocholine (HPC) (phospholipids). 18:1-18:1-C11 TopFluor TG (Avanti Polar Lipids, Birmingham, AL) is a triglyceride conjugated to a fluorophore with similar properties (chemical structure and excitation/emission) as BODIPY and was used to infer the location of triglycerides on TLC plates owing to BODIPY–triglyceride analogs not being commercially available at the time of this publication. Only basal media samples were collected and assessed via TLC from the experiments in Figures 5 and 6. After incubation in solvent, spotted silica gel plates were dried and scanned on an iBright FL 1000 Imager (Invitrogen, Waltham, MA) to detect fluorescent lipid species. Excitation and emission channels were set to 455–485 and 508–557, respectively. A previous study[62] using TLC to identify B-lipid species with the same solvents used in this study reported NFBs that do not correspond to B-lipids.

The chain length of unknown B-labeled fatty acids that appeared in the basal media of absorptive enterocyte cultures was inferred by generating a standard curve of the retention factors of B-FA standards and their chain length. The retention factor of the unknown B-labeled fatty acids was used to interpolate the chain length using the standard curve mentioned previously (Figure 10). The 3 unknown B-FAs corresponded to B-C4, B-C6, and B-C8 (Figure 10).

Microscopy of Primary Human Jejunal Tissue

Post-mortem human jejunal tissue was fixed by incubating in 10% neutral buffered formalin overnight at 4ºC. Tissue was rinsed 3 times in water 3 times the following day and stored in 70% ethanol until embedded. Tissue was embedded in paraffin wax. Glass slides were prepared by sectioning embedded tissue. In situ hybridization was performed using RNAscope probes according to the recommended protocol (Table 3). Images were taken using an LSM710 confocal microscope (Zeiss, Jena, Germany).

Microscopy of 2D Absorptive Enterocyte Monolayers

Absorptive enterocyte monolayers were treated with vehicle or 20 umol/L etomoxir and exposed apically to B-C12 or B-C16 for 6 hours. After 6 hours of apical B-C12 or B-C16 exposure, absorptive enterocyte monolayers were rinsed with fresh DM and fixed in 40% glyoxal solution for 20 minutes. After fixation, absorptive enterocyte monolayers were rinsed with 1× DPBS. Next, the Transwell membrane containing the fixed absorptive enterocyte monolayers were removed from the Transwell inserts and placed on glass slides. Absorptive enterocyte monolayers then were overlaid with mounting media and covered with a glass coverslip. Fluorescent images used for quantification were taken at 20× magnification on an Olympus IX2-UCB (Olympus, Shinjuku City, Tokyo, Japan) microscope. Representative fluorescent images of absorptive enterocyte monolayers in Figure 5 were taken at 40× magnification on a Keyence BZ-X810 microscope (Keyance, Osaka, Japan).

Code and Data Availability

Sequencing data sets will be available on the NCBI Gene Expression Omnibus under accession number GSE186583. Python scripts showing the main parts of our analysis will be available on GitHub.

References

1. Wang TY, Liu M, Portincasa P, Wang DQH. New insights into the molecular mechanism of intestinal fatty acid absorption. Eur J Clin Invest 2013;43:1203–1223.
2. Ko CW, Qu J, Black DD, Tso P. Regulation of intestinal lipid metabolism: current concepts and relevance to disease. Nat Rev Gastroenterol Hepatol 2020; 17:169–183.
3. McDonald GB, Saunders DR, Weidman M, Fisher L. Portal venous transport of long-chain fatty acids absorbed from rat intestine. Am J Physiol Gastrointest Liver Physiol 1980;2:239.
4. Mansbach CM, Dowell RF, Pritchett D. Portal transport of absorbed lipids in rats. Am J Physiol Gastrointest Liver Physiol 1991;261:G530–G538.
5. Mu H, Høy CE. The digestion of dietary triacylglycerols. Prog Lipid Res 2004;43:105–133.
6. Batterink L, Yokum S, Stice E. Body mass correlates inversely with inhibitory control in response to food among adolescent girls: an fMRI study. Neuroimage 2010;52:1696–1703.
7. Donofry SD, Stillman CM, Erickson KI. A review of the relationship between eating behavior, obesity and functional brain network organization. Soc Cogn Affect Neurosci 2020;15:1157–1181.
8. Athyros VG, Doumas M, Imprialos KP, Stavropoulos K, Georgianou E, Katsimardou A, Karagiannis A. Diabetes and lipid metabolism. Hormones 2018;17:61–67.

9. Glovaci D, Fan W, Wong ND. Epidemiology of diabetes mellitus and cardiovascular disease. Curr Cardiol Rep 2019;21:21.

10. van Rijn JM, Ardy RC, Kuloğlu Z, Härter B, van Haaften-Visser DY, van der Doef HPJ, van Hoesel M, Kansu A, van Vugt AHM, Thian M, Kokke FTM, Krolo A, Başaran MK, Kaya NG, Aksu AÜ, Dalgıç B, Ozcay F, Baris Z, Kain R, Stigter ECA, Lichtenbelt KD, Massink MPG, Duran KJ, Verheij JBGM, Lugtenberg D, Nikkels PGJ, Brouwer HGF, Verkade HJ, Scheenstra R, Spee B, Nieuwenhuis EES, Coffer PJ, Janecke AR, van Haaften G, Houwen RHJ, Müller T, Middendorp S, Boztug K. Intestinal failure and aberrant lipid metabolism in patients with DGAT1 deficiency. Gastroenterology 2018;155:130–143.e15.

11. Luglio HF. Genetic variation of fatty acid oxidation and obesity, a literature review. Int J Biomed Sci 2016; 12:1–8.

12. McCann JR, Bihlmeyer NA, Roche K, Catherine C, Jawahar J, Kwee LC, Younge NE, Silverman J, Ilkayeva O, Sarria C, Zizzi A, Wootton J, Poppe L, Anderson P, Arlotto M, Wei Z, Granek JA, Valdivia RH, David LA, Dressman HK, Newgard CB, Shah SH, Seed PC, Rawls JF, Armstrong SC. The Pediatric Obesity Microbiome and Metabolism Study (POMMS): methods, baseline data, and early insights. Obesity 2021;29:569–578.

13. Jumpertz R, Le DS, Turnbaugh PJ, Trinidad C, Bogardus C, Gordon JI, Krakoff J. Energy-balance studies reveal associations between gut microbes, caloric load, and nutrient absorption in humans. Am J Clin Nutr 2011;94:58–65.

14. Nagpal R, Wang S, Solberg Woods LC, Seshie O, Chung ST, Shively CA, Register TC, Craft S, McClain DA, Yadav H. Comparative microbiome signatures and short-chain fatty acids in mouse, rat, non-human primate, and human feces. Front Microbiol 2018;9:2897.

15. Ridaura VK, Faith JJ, Rey FE, Cheng J, Duncan AE, Kau AL, Griffin NW, Lombard V, Henrissat B, Bain JR, Muehlbauer MJ, Ilkayeva O, Semenkovich CF, Funai K, Hayashi DK, Lyle BJ, Martini MC, Ursell LK, Clemente JC, Van Treuren W, Walters WA, Knight R, Newgard CB, Heath AC, Gordon JI. Gut microbiota from twins discordant for obesity modulate metabolism in mice. Science 2013;341:1241214.

16. Trotter PJ, Ho SY, Storch J. Fatty acid uptake by Caco-2 human intestinal cells. J Lipid Res 1996;37:336–346.

17. Bens M, Bogdanova A, Cluzeaud F, Miquerol L, Kerneis S, Kraehenbuhl JP, Kahn A, Pringault E, Vandewalle A. Transimmortalized mouse intestinal cells (m-IC(cl2)) that maintain a crypt phenotype. Am J Physiol Cell Physiol 1996;270:C1666–C1674.

18. Pandrea IV, Carrière V, Barbat A, Cambier D, Dussaulx E, Lesuffleur T, Rousset M, Zweibaum A. Postmitotic differentiation of colon carcinoma Caco-2 cells does not prevent reentry in the cell cycle and tumorigenicity. Exp Mol Pathol 2000;69:37–45.

19. Sun H, Chow ECY, Liu S, Du Y, Pang KS. The Caco-2 cell monolayer: usefulness and limitations. Expert Opin Drug Metab Toxicol 2008;4:395–411.

20. Rahman S, Ghiboub M, Donkers JM, Steeg E van de, Tol EAF van, Hakvoort TBM, Jonge WJ de. The progress of intestinal epithelial models from cell lines to gut-on-chip. Int J Mol Sci 2021;22:13472.

21. Schutgens F, Clevers H. Human organoids: tools for understanding biology and treating diseases. Annu Rev Pathol 2020;15:211–234.

22. Sato T, Vries RG, Snippert HJ, Van De Wetering M, Barker N, Stange DE, Van Es JH, Abo A, Kujala P, Peters PJ, Clevers H. Single Lgr5 stem cells build crypt-villus structures in vitro without a mesenchymal niche. Nature 2009;459:262–265.

23. Co JY, Margalef-Català M, Li X, Mah AT, Kuo CJ, Monack DM, Amieva MR. Controlling epithelial polarity: a human enteroid model for host-pathogen interactions. Cell Rep 2019;26:2509–2520.e4.

24. Rumjanek FD, Simpson AJG. The incorporation and utilization of radiolabelled lipids by adult Schistosoma mansoni in vitro. Mol Biochem Parasitol 1980; 1:31–44.

25. Murphy JL, Jones A, Brookes S, Wootton SA. The gastrointestinal handling and metabolism of [1-13C] palmitic acid in healthy women. Lipids 1995;30:291–298.

26. Kalivianakis M, Verkade HJ, Stellaard F, Van Der Werf M, Elzinga H, Vonk RJ. The 13C-mixed triglyceride breath test in healthy adults: determinants of the 13CO2 response. Eur J Clin Invest 1997;27:434–442.

27. Hofmann M, Eichenberger W. Radiolabelling studies on the lipid metabolism in the marine brown alga dictyopteris membranacea. Plant Cell Physiol 1998;39:508–515.

28. Ecker J, Liebisch G. Application of stable isotopes to investigate the metabolism of fatty acids, glycerophospholipid and sphingolipid species. Prog Lipid Res 2014;54:14–31.

29. Triebl A, Wenk MR. Analytical considerations of stable isotope labelling in lipidomics. Biomolecules 2018;8:151.

30. Twining CW, Taipale SJ, Ruess L, Bec A, Martin-Creuzburg D, Kainz MJ. Stable isotopes of fatty acids: current and future perspectives for advancing trophic ecology. Philos Trans R Soc B Biol Sci 2020; 375:20190641.

31. Maier O, Oberle V, Hoekstra D. Fluorescent lipid probes: some properties and applications (a review). Chem Phys Lipids 2002;116:3–18.

32. Johnson ID, Kang HC, Haugland RP. Fluorescent membrane probes incorporating dipyrrometheneboron difluoride fluorophores. Anal Biochem 1991; 198:228–237.

33. Bergström F, Mikhalyov I, Hägglöf P, Wortmann R, Ny R, Johansson LB-Å. Dimers of dipyrrometheneboron difluoride (BODIPY) with light spectroscopic applications in chemistry and biology. J Am Chem Soc 2001; 124:196–204.

34. Valm AM, Cohen S, Legant WR, Melunis J, Hershberg U, Wait E, Cohen AR, Davidson MW, Betzig E, Lippincott-Schwartz J. Applying systems-level spectral imaging and analysis to reveal the organelle interactome. Nature 2017;546:162–167.

35. Rambold AS, Cohen S, Lippincott-Schwartz J. Fatty acid trafficking in starved cells: regulation by lipid droplet lipolysis, autophagy, and mitochondrial fusion dynamics. Dev Cell 2015;32:678–692.

36. Wang Y, DiSalvo M, Gunasekara DB, Dutton J, Proctor A, Lebhar MS, Williamson IA, Speer J, Howard RL, Smiddy NM, Bultman SJ, Sims CE, Magness ST, Allbritton NL. Self-renewing monolayer of primary colonic or rectal epithelial cells. Cell Mol Gastroenterol Hepatol 2017;4:165–182.e7.

37. Hinman SS, Wang Y, Kim R, Allbritton NL. In vitro generation of self-renewing human intestinal epithelia over planar and shaped collagen hydrogels. Nat Protoc 2020; 16:352–382.

38. Lema I, Araújo JR, Rolhion N, Demignot S. Jejunum: the understudied meeting place of dietary lipids and the microbiota. Biochimie 2020;178:124–136.

39. Busslinger GA, Weusten BLA, Bogte A, Begthel H, Brosens LA, Clevers H. Human gastrointestinal epithelia of the esophagus, stomach, and duodenum resolved at single-cell resolution. Cell Rep 2021;34:108819.

40. Wang Y, Song W, Wang J, Wang T, Xiong X, Qi Z, Fu W, Yang X, Chen Y-G. Single-cell transcriptome analysis reveals differential nutrient absorption functions in human intestine. J Exp Med 2020;217:e20191130.

41. Elmentaite R, Kumasaka N, Roberts K, Fleming A, Dann E, King HW, Kleshchevnikov V, Dabrowska M, Pritchard S, Bolt L, Vieira SF, Mamanova L, Huang N, Perrone F, Goh Kai'En I, Lisgo SN, Katan M, Leonard S, Oliver TRW, Hook CE, Nayak K, Campos LS, Domínguez Conde C, Stephenson E, Engelbert J, Botting RA, Polanski K, van Dongen S, Patel M, Morgan MD, Marioni JC, Bayraktar OA, Meyer KB, He X, Barker RA, Uhlig HH, Mahbubani KT, Saeb-Parsy K, Zilbauer M, Clatworthy MR, Haniffa M, James KR, Teichmann SA. Cells of the human intestinal tract mapped across space and time. Nature 2021;597:250–255.

42. Burclaff J, Bliton RJ, Breau KA, et al. A proximal-to-distal survey of healthy adult human small intestine and colon epithelium by single-cell transcriptomics. CMGH 2022;13(5):1554–1589. https://doi.org/10.1101/2021.10.05.460818.

43. Traag VA, Waltman L, van Eck NJ. From Louvain to Leiden: guaranteeing well-connected communities. Sci Rep 2019;9:1–12.

44. Barker N, Van Es JH, Kuipers J, Kujala P, Van Den Born M, Cozijnsen M, Haegebarth A, Korving J, Begthel H, Peters PJ, Clevers H. Identification of stem cells in small intestine and colon by marker gene Lgr5. Nature 2007;449:1003–1007.

45. Triana S, Stanifer ML, Metz-Zumaran C, Shahraz M, Mukenhirn M, Kee C, Serger C, Koschny R, Ordoñez-Rueda D, Paulsen M, Benes V, Boulant S, Alexandrov T. Single-cell transcriptomics reveals immune response of intestinal cell types to viral infection. Mol Syst Biol 2021; 17:9833.

46. Tirosh I, Izar B, Prakadan SM, Wadsworth MH, Treacy D, Trombetta JJ, Rotem A, Rodman C, Lian C, Murphy G, Fallahi-Sichani M, Dutton-Regester K, Lin J-R, Cohen O, Shah P, Lu D, Genshaft AS, Hughes TK, Ziegler CGK, Kazer SW, Gaillard A, Kolb KE, Villani A-C, Johannessen CM, Andreev AY, Allen EM Van, Bertagnolli M, Sorger PK, Sullivan RJ, Flaherty KT, Frederick DT, Jané-Valbuena J, Yoon CH, Rozenblatt-Rosen O, Shalek AK, Regev A, Garraway LA. Dissecting the multicellular ecosystem of metastatic melanoma by single-cell RNA-seq. Science 2016;352:189–196.

47. Muñoz J, Stange DE, Schepers AG, Wetering M van de, Koo B-K, Itzkovitz S, Volckmann R, Kung KS, Koster J, Radulescu S, Myant K, Versteeg R, Sansom OJ, Es JH van, Barker N, Oudenaarden A van, Mohammed S, Heck AJR, Clevers H. The Lgr5 intestinal stem cell signature: robust expression of proposed quiescent '+4'' cell markers. ' EMBO J 2012;31:3079.

48. Gracz AD, Ramalingam S, Magness ST. Sox9 expression marks a subset of CD24-expressing small intestine epithelial stem cells that form organoids in vitro. Am J Physiol Gastrointest Liver Physiol 2010;298:G590.

49. Moor AE, Harnik Y, Ben-Moshe S, Massasa EE, Rozenberg M, Eilam R, Bahar Halpern K, Itzkovitz S. Spatial reconstruction of single enterocytes uncovers broad zonation along the intestinal villus axis. Cell 2018; 175:1156–1167.e15.

50. La Manno G, Soldatov R, Zeisel A, Braun E, Hochgerner H, Petukhov V, Lidschreiber K, Kastriti ME, Lönnerberg P, Furlan A, Fan J, Borm LE, Liu Z, van Bruggen D, Guo J, He X, Barker R, Sundström E, Castelo-Branco G, Cramer P, Adameyko I, Linnarsson S, Kharchenko PV. RNA velocity of single cells. Nature 2018;560:494–498.

51. Bergen V, Lange M, Peidli S, Wolf FA, Theis FJ. Generalizing RNA velocity to transient cell states through dynamical modeling. Nat Biotechnol 2020; 38:1408–1414.

52. Speer JE, Gunasekara DB, Wang Y, Fallon JK, Attayek PJ, Smith PC, Sims CE, Allbritton NL. Molecular transport through primary human small intestinal monolayers by culture on a collagen scaffold with a gradient of chemical cross-linking. J Biol Eng 2019;13:36.

53. Demitrack ES, Samuelson LC. Notch regulation of gastrointestinal stem cells. J Physiol 2016; 594:4791–4803.

54. Shroyer NF, Helmrath MA, Wang VY-C, Antalffy B, Henning SJ, Zoghbi HY. Intestine-specific ablation of mouse atonal homolog 1 (Math1) reveals a role in cellular homeostasis. Gastroenterology 2007; 132:2478–2488.

55. Srinivasan B, Kolli AR, Esch MB, Abaci HE, Shuler ML, Hickman JJ. TEER measurement techniques for in vitro barrier model systems. J Lab Autom 2015;20:107.

56. Wang Y, Kim R, Hwang SHJ, Dutton J, Sims CE, Allbritton NL. Analysis of interleukin 8 secretion by a stem-cell-derived human-intestinal-epithelial-monolayer platform. Anal Chem 2018;90:11523–11530.

57. Furse S, De Kroon AIPM. Phosphatidylcholines functions beyond that of a membrane brick. Mol Membr Biol 2015; 32:117–119.

58. Otis JP, Farber SA. Imaging vertebrate digestive function and lipid metabolism in vivo. Drug Discov Today Dis Model 2013;10(1).

59. Anderson JL, Carten JD, Farber SA. Using fluorescent lipids in live zebrafish larvae: from imaging whole animal physiology to subcellular lipid trafficking. Methods Cell Biol 2016;133:165.

60. Semova I, Carten JD, Stombaugh J, MacKey LC, Knight R, Farber SA, Rawls JF. Microbiota regulate intestinal absorption and metabolism of fatty acids in the zebrafish. Cell Host Microbe 2012;12:277–288.

61. Sæle Ø, Rød KEL, Quinlivan VH, Li S, Farber SA. A novel system to quantify intestinal lipid digestion and transport. Biochim Biophys Acta Mol Cell Biol Lipids 2018; 1863:948–957.

62. Carten JD, Bradford MK, Farber SA. Visualizing digestive organ morphology and function using differential fatty acid metabolism in live zebrafish. Dev Biol 2011;360:276.

63. Houten SM, Violante S, Ventura FV, Wanders RJA. The biochemistry and physiology of mitochondrial fatty acid β-oxidation and its genetic disorders. Annu Rev Physiol 2016;78:23–44.

64. Yao CH, Liu GY, Wang R, Moon SH, Gross RW, Patti GJ. Identifying off-target effects of etomoxir reveals that carnitine palmitoyltransferase i is essential for cancer cell proliferation independent of β-oxidation. PLoS Biol 2018; 16:e2003782.

65. Divakaruni AS, Hsieh WY, Minarrieta L, Duong TN, Kim KKO, Desousa BR, Andreyev AY, Bowman CE, Caradonna K, Dranka BP, Ferrick DA, Liesa M, Stiles L, Rogers GW, Braas D, Ciaraldi TP, Wolfgang MJ, Sparwasser T, Berod L, Bensinger SJ, Murphy AN. Etomoxir inhibits macrophage polarization by disrupting CoA homeostasis. Cell Metab 2018;28:490–503.e7.

66. Raud B, Roy DG, Divakaruni AS, Tarasenko TN, Franke R, Ma EH, Samborska B, Hsieh WY, Wong AH, Stüve P, Arnold-Schrauf C, Guderian M, Lochner M, Rampertaap S, Romito K, Monsale J, Brönstrup M, Bensinger SJ, Murphy AN, McGuire PJ, Jones RG, Sparwasser T, Berod L. Etomoxir actions on regulatory and memory T cells are independent of Cpt1a-mediated fatty acid oxidation. Cell Metab 2018;28:504–515.e7.

67. Khuwijitjaru P, Adachi S, Matsuno R. Solubility of saturated fatty acids in water at elevated temperatures materials and methods. Biosci Biotechnol Biochem 2002; 66:1723–1726.

68. Thupari JN, Landree LE, Ronnett GV, Kuhajda FP. C75 increases peripheral energy utilization and fatty acid oxidation in diet-induced obesity. Proc Natl Acad Sci U S A 2002;99:9498–9502.

69. Wang C, Liu F, Yuan Y, Wu J, Wang H, Zhang L, Hu P, Li Z, Li Q, Ye J. Metformin suppresses lipid accumulation in skeletal muscle by promoting fatty acid oxidation. Clin Lab 2014;60:887–896.

70. Zabielski P, Chacinska M, Charkiewicz K, Baranowski M, Gorski J, Blachnio-Zabielska AU. Effect of metformin on bioactive lipid metabolism in insulin-resistant muscle. J Endocrinol 2017;233:329–340.

71. Kuncewitch M, Yang WL, Jacob A, Khader A, Giangola M, Nicastro J, Coppa GF, Wang P. Inhibition of fatty acid synthase with C75 decreases organ injury after hemorrhagic shock. Surgery 2016;159:570–579.

72. Zachos NC, Kovbasnjuk O, Foulke-Abel J, In J, Blutt SE, Jonge HR de, Estes MK, Donowitz M. Human enteroids/colonoids and intestinal organoids functionally recapitulate normal intestinal physiology and pathophysiology. J Biol Chem 2016;291:3759.

73. Raab JR, Tulasi DY, Wager KE, Morowitz JM, Magness ST, Gracz AD. Quantitative classification of chromatin dynamics reveals regulators of intestinal stem cell differentiation. Development 2020;147:dev181966.

74. Kim T-H, Li F, Ferreiro-Neira I, Ho L-L, Luyten A, Nalapareddy K, Long H, Verzi M, Shivdasani RA. Broadly permissive intestinal chromatin underlies lateral inhibition and cell plasticity. Nature 2014;506:511.

75. Carlier H, Bezard J. Electron microscope autoradiographic study of intestinal absorption of decanoic and octanoic acids in the rat. J Cell Biol 1975;65:383–397.

76. Ways PO, Parmentier CM, Kayden HJ, Jones JW, Saunders DR, Rubin CE. Studies on the absorptive defect for triglyceride in abetalipoproteinemia. J Clin Invest 1967;46:35–46.

77. Christensen LW, Kuhre RE, Janus C, Svendsen B, Holst JJ. Vascular, but not luminal, activation of FFAR1 (GPR40) stimulates GLP-1 secretion from isolated perfused rat small intestine. Physiol Rep 2015;3:e12551.

78. Kimura I, Ichimura A, Ohue-Kitano R, Igarashi M. Free fatty acid receptors in health and disease. Physiol Rev 2020;100:171–210.

79. Bahne E, Sun EWL, Young RL, Hansen M, Sonne DP, Hansen JS, Rohde U, Liou AP, Jackson ML, de Fontgalland D, Rabbitt P, Hollington P, Sposato L, Due S, Wattchow DA, Rehfeld JF, Holst JJ, Keating DJ, Vilsbøll T, Knop FK. Metformin-induced glucagon-like peptide-1 secretion contributes to the actions of metformin in type 2 diabetes. JCI Insight 2018;3:e93936.

80. Mulherin AJ, Oh AH, Kim H, Grieco A, Lauffer LM, Brubaker PL. Mechanisms underlying metformin-induced secretion of glucagon-like peptide-1 from the intestinal L cell. Endocrinology 2011;152:4610–4619.

81. Kowalczyk MS, Tirosh I, Heckl D, Rao TN, Dixit A, Haas BJ, Schneider RK, Wagers AJ, Ebert BL, Regev A. Single-cell RNA-seq reveals changes in cell cycle and differentiation programs upon aging of hematopoietic stem cells. Genome Res 2015;25:1860.

82. Wolf FA, Angerer P, Theis FJ. SCANPY: large-scale single-cell gene expression data analysis. Genome Biol 2018;19:1–5.

83. Satija R, Farrell J, Gennert D, Schier A, Regev A. Spatial reconstruction of single-cell gene expression data. Nature Biotechnology 2015;33:495–502. https://doi.org/10.1038/nbt.3192.

84. Wolf FA, Hamey FK, Plass M, Solana J, Dahlin JS, Göttgens B, Rajewsky N, Simon L, Theis FJ. PAGA: graph abstraction reconciles clustering with trajectory inference through a topology preserving map of single cells. Genome Biol 2019;20:1–9.

85. McInnes L, Healy J, Melville J. UMAP: Uniform Manifold Approximation and Projection for Dimension

Reduction. arXiv 2018. https://doi.org/10.48550/arXiv.1802.03426.

86. Virshup I, Rybakov S, Theis F, Angerer P, Wolf FA. anndata: Annotated data. bioRxiv 2021. https://doi.org/10.1101/2021.12.16.473007.

87. Fischer DS, Hölzlwimmer FR, Eraslan G, Heumos L. Fast and scalable differential expression analysis on single-cell RNA-seq data, Available from: https://github.com/theislab/diffxpy. 2020. Accessed March 24, 2021.

88. Schroeder A, Mueller O, Stocker S, Salowsky R, Leiber M, Gassmann M, Lightfoot S, Menzel W, Granzow M, Ragg T. The RIN: an RNA integrity number for assigning integrity values to RNA measurements. BMC Mol Biol 2006;7:3.

89. Bray NL, Pimentel H, Melsted P, Pachter L. Near-optimal probabilistic RNA-seq quantification. Nat Biotechnol 2016;34:525–527.

90. Robinson MD, Oshlack A. A scaling normalization method for differential expression analysis of RNA-seq data. Genome Biol 2010;11:R25.

91. Robinson M, McCarthy D, Smyth G. edgeR: a Bioconductor package for differential expression analysis of digital gene expression data. Bioinformatics 2010;26. https://doi.org/10.1093/bioinformatics/btp616.

92. Pedregosa, et al. Scikit-learn: Machine Learning in Python. The Journal of Machine Learning 2011.

93. Sündermann A, Eggers LF, Schwudke D. Liquid extraction: Bligh and Dyer. Encycl Lipidomics 2016;1–4.

Correspondence
Address correspondence to: Scott T. Magness, PhD, Department of Biomedical Engineering, University of North Carolina at Chapel Hill, 111 Mason Farm Road, Chapel Hill, North Carolina 27599. e-mail: magness@med.unc.edu.